

# 1 **Effective killing of bacteria under blue-light irradiation promoted by green** 2 **synthesized silver nanoparticles loaded on reduced graphene oxide sheets**

3 Cynthia S. A. Caires,<sup>a,b†</sup> Luiz A. S. Farias,<sup>c†</sup> Luiz E. Gomes,<sup>c</sup> Bruno P. Pinto,<sup>c</sup> Daniel A. Gonçalves,<sup>a,d</sup> Luiz F.  
4 Zagonel,<sup>e</sup> Valter A. Nascimento,<sup>a</sup> Diego C. B. Alves,<sup>c</sup> Ian Colbeck<sup>b</sup>, Corinne Whitby<sup>b</sup>, Anderson R. L. Caires<sup>b,f,\*</sup>  
5 and Heberton Wender<sup>c\*</sup>

6  
7 <sup>a</sup> Laboratory of Spectroscopy and Bioinformatics Applied to Biodiversity and Health, Faculty of Medicine,  
8 Federal University of Mato Grosso do Sul, Campo Grande, Mato Grosso do Sul, 79070-900, Brazil.

9 <sup>b</sup> School of Life Sciences, University of Essex, Colchester, CO4 3SQ, UK.

10 <sup>c</sup> Laboratory of Nanomaterials and Applied Nanotechnology (LNNA), Institute of Physics, Federal University of  
11 Mato Grosso do Sul, Campo Grande, Mato Grosso do Sul, 79070-900, Brazil.

12 <sup>d</sup> Department of Chemistry, Minas Gerais State University - UEMG, Ituiutaba, MG 38302-192, Brazil.

13 <sup>e</sup> “Gleb Wataghin” Institute of Physics, University of Campinas – UNICAMP, 13083-859 Campinas, São Paulo,  
14 Brazil.

15 <sup>f</sup> Laboratory of Optic and Photonics, Institute of Physics, Federal University of Mato Grosso do Sul, Campo  
16 Grande, Mato Grosso do Sul, 79070-900, Brazil.

## 17 **Abstract**

18 Graphene oxide (GO) materials loaded with silver nanoparticles (AgNPs) have drawn  
19 considerable attention due to their capacity to efficiently inactivate bacteria though a  
20 multifaceted mechanism of action, as well as for presenting a synergetic effect against  
21 bacteria when compared to the activity of AgNPs and GO alone. In this investigation,  
22 we present an inexpensive and environmentally-friendly method for synthesizing  
23 reduced GO sheets coated with silver nanoparticles (AgNPs/r-GO) using a coffee extract  
24 solution as a green reducing agent. The physical and chemical properties of the produced  
25 materials were extensively characterized by scanning electron microscopy (SEM), field-  
26 emission gun transmission electron microscopy (FEG-TEM), ultraviolet and visible  
27 absorption (UV-Vis), Raman spectroscopy, X-ray photoelectron spectroscopy (XPS),

28 inductively coupled plasma-optical emission spectroscopy (ICP-OES) and ion release  
29 determination. The results demonstrated that AgNPs/r-GO composites were  
30 successfully produced, revealing the formation of micrometer-sized r-GO sheets  
31 decorated by AgNPs of approximately 70 nm diameter. Finally, bactericidal and  
32 photobactericidal effects of the AgNPs/r-GO composites were tested against  
33 *Staphylococcus aureus*, in which the results showed that the composites presented  
34 antimicrobial and photoantimicrobial activities. Moreover, our results demonstrated for  
35 the first time, to our knowledge, that an efficient process of bacterial inactivation can be  
36 achieved by using AgNPs/r-GO composites under blue light irradiation as a result of  
37 three different bacterial killing processes: (i) chemical effect promoted by Ag<sup>+</sup> ion  
38 release from AgNPs; (ii) photocatalytic activity induced by AgNPs/r-GO composites,  
39 enhancing the bacterial photoinactivation due to the excited-Plasmons of the AgNPs  
40 when anchored on r-GO; and (iii) photodynamic effect produced by bacterial  
41 endogenous photosensitizers under blue-light irradiation. In summary, the present  
42 findings demonstrated that AgNPs/r-GO can be obtained by a non-toxic procedure with  
43 great potential for biomedical-related applications.

44 Keywords: Green synthesis; Silver nanoparticle; Reduced graphene oxide; Blue light  
45 irradiation; Photoinactivation; *Staphylococcus aureus*.

46 † These authors contributed equally to this work.

47 \* Corresponding authors: [heberton.wender@ufms.br](mailto:heberton.wender@ufms.br); [anderson.caires@ufms.br](mailto:anderson.caires@ufms.br)

48

## 49 **1. INTRODUCTION**

50 Ag-based nanomaterials have attracted the attention in a wide variety of applications,  
51 due to their unique chemical, biological, and physical properties, allowing their use  
52 predominantly in health care and related fields [1–6]. Among the Ag-based compounds,  
53 silver nanoparticles (AgNPs) are of special interest due to their high surface area and

54 specific Surface Plasmon Resonance (SPR) effect [7,8]. Chemical reduction is the most  
55 frequently applied methods for the preparation of AgNPs in the form of stable colloidal  
56 solutions in water or organic solvents [9]. However, AgNP production has to address  
57 environmental issues and biocompatibility by using “green” methodologies because  
58 toxic products such as citrate, borohydride, ascorbate, and H<sub>2</sub> are the most commonly  
59 used reducing agents for the synthesis of AgNPs [10]. In this scenario, environmentally  
60 friendly plant extracts, such as dried berries [5], seeds [11], leaves [12], and fruits [13]  
61 have been proposed as efficient and clean chemical reductants for synthesizing AgNPs.  
62 Recently, coffee extract was suggested as a natural reductant for the preparation of  
63 AgNPs under room temperature conditions because it contains caffeine and polyphenols  
64 in their chemical composition which drives the reduction of metallic Ag ions in water  
65 [4,14,15].

66 Among several possible applications of AgNPs, their efficacy to inactivate both  
67 Gram-positive and Gram-negative bacteria has been subject to increased attention  
68 because AgNPs and Ag ions (Ag<sup>+</sup>) released by AgNPs present a multifaceted  
69 mechanism of action against bacteria [16]. This allows AgNPs to efficiently kill  
70 antibiotic-resistant bacteria as well as their multifaceted action makes difficult the  
71 development of resistance by the bacteria [17]. The emergence of multi-drug resistant  
72 bacteria has become one of the major challenges in public health as a consequence of  
73 inappropriate and excessive use of antibiotics in clinics, hospitals, and animal and food  
74 industries [18–20]. In this scenario, it is necessary to develop new technologies for the  
75 treatment of multidrug-resistant bacteria [21–27]. Recent advances have demonstrated  
76 that a wide range of nanomaterials can be used as inorganic antimicrobial agents [28].  
77 For instance, microbial inactivation can be achieved by using functional nanomaterials

78 composed of silver, zinc, copper and metal oxide nanoparticles due to their unique  
79 antibacterial properties [28].

80 The antibacterial effects of AgNPs are mainly attributed to  $\text{Ag}^+$  release from the  
81 nanoparticle surface, which can penetrate into bacterial cells and, consequently, damage  
82 or even kill the microorganisms by preventing their replication abilities [29,30]. The  
83  $\text{Ag}^+$  bactericidal mechanism is attributed to the combination of two interacting  
84 processes: (i) the capacity of the ions to interact with thiol groups in proteins, inducing  
85 their inactivation; and (ii) the ions' interaction with bacterial DNA, condensing the DNA  
86 and preventing DNA replication [30].

87 Graphene oxide (GO) is formed by carbon sheets that have functional groups of  
88 oxygen, leading to a good dispersion in polar solvents, for example in water [31]. This  
89 feature enables the deposition of NPs on their surface, resulting in a composite material  
90 that can be used in various applications [32–34]. Recent studies have demonstrated that  
91 GO can be used as a platform for AgNPs, presenting high mechanical strength, large  
92 surface area, fast charge transfer, and good biocompatibility [35]. It has also been  
93 demonstrated that GO can present antibacterial properties [6,36] and there may exist a  
94 synergism between Ag and GO when AgNPs are incorporated into GO, enhancing the  
95 antibacterial properties of the GO/AgNPs composites [30]. Although the antibacterial  
96 effect of GO/AgNPs may be higher than that of a single GO or AgNPs, the major  
97 mechanism for bacteria-killing is still attributed to the  $\text{Ag}^+$  release [30].

98 Furthermore, in addition to the chemical bactericidal properties, AgNPs can act as  
99 photobactericidal agents due to their capacity to absorb light in the visible range,  
100 producing reactive oxygen species (ROS) by photodynamic processes [37]. The  
101 photosensitizer properties of the AgNPs originate from the existence of the SPR band  
102 due to the collective electron oscillations on the nanoparticle surface [7,8], which is

103 usually in the 400 to 490 nm range (blue region) when in a spherical shape. In fact, the  
104 photoantimicrobial effect of AgNPs can take place as free electrons can be produced  
105 during the SPR induced by the light irradiation, leading to a large amount of ROS and,  
106 consequently, killing bacteria [38]. In addition, recent results have also demonstrated  
107 that the photoinactivation activity of some nanoparticles can be enhanced when  
108 anchored on GO sheets, allowing the free electrons originated from the NPs be rapidly  
109 transferred to the surface of GO and then move through the nanosheets, where ROS are  
110 produced [28,38–40]. It worth pointing out that this possibility of moving on the GO  
111 surface enhances the probability of the free electron finding and interacting with  
112 molecular oxygen and thus increasing the photoantimicrobial activity of AgNPs [38].

113 In this paper, we present an inexpensive, environmentally friendly process for  
114 synthesizing AgNPs anchored on r-GO sheets by using a coffee extract solution as a  
115 green reducing agent at room temperature. Bactericidal and photobactericidal activities  
116 under blue-light irradiation of the AgNPs/r-GO composites were tested against  
117 *Staphylococcus aureus* strain, revealing that a synergetic antimicrobial effect can be  
118 obtained when compared to the results of AgNPs and r-GO. In fact, the present study  
119 aims to present, for the first time that an efficient process of bacterial inactivation can  
120 be performed using AgNPs/r-GO composites as a consequence of three different  
121 bacterial killing mechanisms that can be achieved simultaneously by AgNPs/r-GO  
122 under blue-light illumination, such as Ag<sup>+</sup> ion release (chemical effect induced by  
123 AgNPs), enhanced photoinactivation promoted by excited-Plasmons of the AgNPs  
124 when anchored on r-GO (photocatalytic activity promoted by AgNPs/r-GO composites),  
125 and blue-light photodynamic inactivation caused by bacterial endogenous  
126 photosensitizers (photodynamic effect produced by bacterial endogenous  
127 photosensitizers).

## 128 2. MATERIALS AND METHODS

129 **2.1. GO synthesis.** Before the composite synthesis, GO was prepared using the  
130 modified Hummers' methods [31]. GO concentration was determined at 0.74 mg/mL ( $\pm$   
131 7.8 %) and used as a stock solution for all samples prepared in this work. More details  
132 can be accessed in the Supplementary Material.

133

134 **2.2. Preparation and characterization of the coffee extract.** 400 mg of, as obtained,  
135 black coffee powder (Brasileiro®, Brazil) was added to 50 mL of distilled water  
136 (conductivity of 0.05  $\mu\text{S}\cdot\text{cm}^{-1}$ ) and heated up to 70°C for 20 min, under magnetic  
137 stirring. After cooling to room temperature, the powder was removed using a filter paper  
138 and thus the aqueous extract of black coffee was stored at 5-10°C for further  
139 experiments. The chemical composition of the coffee extract was studied by high-  
140 performance liquid chromatography (HPLC) in a Shimadzu equipment model  
141 Prominence 20A with a quaternary pump, automatic sampler, and DAD detector. The  
142 chromatographic method was developed and optimized in which the improved  
143 conditions were: mobile phase methanol/water (60/40) at pH 3.0, chromatographic  
144 column Eclipse C18 150 cm x 4.6 mm, 4.5  $\mu\text{m}$  and a wavelength of 325 nm (caffeine)  
145 and 350 nm (caffeic acid), flow of 0.6 mL $\cdot\text{min}^{-1}$ , injection volume of 5  $\mu\text{L}$  and oven  
146 temperature of 400°C and analysis time of 8 minutes. The presence of caffeine and  
147 caffeic acid was proven using a standard through analysis of the UV spectrum in the  
148 wavelengths of 325 and 350 nm, respectively.

149

150 **2.3. Green synthesis of AgNPs.** AgNPs were prepared using the procedure reported by  
151 Nadagouda and Varma [4] with few modifications. In brief, the AgNPs were produced  
152 by adding 2 mL of a 0.1M  $\text{AgNO}_3$  (99.5 % of purity) solution to 10 mL of coffee, kept

153 under magnetic agitation at room temperature and ambient pressure for 2h. After  
154 preparation, the final solution was stored between 2 – 5°C.

155

156 **2.4. *In situ* synthesis of AgNPs/r-GO nanocomposites.** Two methods were used for  
157 the synthesis of the AgNPs/r-GO composites. The first sample (AgNPs/r-GO<sub>#1</sub>) was  
158 prepared as follows: 2 mL of 0.1M AgNO<sub>3</sub> was added to 10 mL of the coffee solution  
159 under agitation for 15 minutes. Next, 2 mL of the prepared GO solution was added to  
160 the previous mixture. The reaction was maintained under stirring for 2h at room  
161 temperature. The second sample (AgNPs/r-GO<sub>#2</sub>) was prepared by changing the  
162 procedure order, i.e., by first mixing and stirring the GO and coffee extract solutions for  
163 15 min and then AgNO<sub>3</sub> solution (2 mL at 0.1M) was added and stirred for 2 h at room  
164 temperature.

165

166 **2.5. AgNPs, GO and AgNPs/r-GO characterization.** The morphology of GO was  
167 studied in a JEOL scanning electron microscope (SEM) model JSM6380-LV and in a  
168 FEI field-emission gun transmission electron microscope (FEG-TEM) model Quanta  
169 3D operated in the STEM mode. For the collection of images, GO samples were  
170 dispersed in ethanol and sonicated for 20 min prior to depositing onto a holey carbon  
171 copper grid and drying at room temperature. Morphological and crystalline features of  
172 AgNPs and AgNPs/r-GO composites were investigated in a field-emission gun  
173 transmission electron microscope (FEG-TEM) model JEM2100 operated at 200 kV. The  
174 AgNPs or AgNPs/r-GO aqueous samples were dispersed in ethanol at room temperature  
175 and then deposited onto a 400 mesh carbon-coated Cu grid. The histograms of the  
176 nanoparticle size distribution, assuming a spherical shape were obtained from  
177 measurements of more than 200 particles found in arbitrarily chosen regions of the grid.

178 The histograms of the NPs were fitted considering a normal distribution. Ultraviolet and  
179 visible (UV-Vis) spectrophotometry was performed in the 200 - 700 nm range in a  
180 PerkinElmer model Lambda 265. X-ray Photoelectron Spectroscopy (XPS) analyses  
181 were performed using a conventional XPS spectrometer (Scienta Omicron ESCA+) with  
182 a high-performance hemispheric analyser (EAC2000) with monochromatic Al K $\alpha$  ( $h\nu$   
183 = 1486.6 eV) radiation as the excitation source. The operating pressure during the  
184 analysis was  $10^{-9}$  Pa and XPS high-resolution spectra were recorded at constant pass  
185 energy of 20 eV with a 0.05 eV per step. Peak positions were corrected by C 1s  
186 adventitious carbon set at 284.8 eV using the CasaXPS software package for the  
187 treatment of the acquired spectra. Raman spectra at room temperature were recorded  
188 using an alpha 300 RA  $\mu$ -Raman microscope (WITec, Ulm, Germany), in a  
189 backscattering geometry with 600  $\text{gr}\cdot\text{mm}^{-1}$  holographic gratings, in the wavenumber  
190 range between 100 and 1500  $\text{cm}^{-1}$ . An argon ion laser operating at 633 nm was used as  
191 an excitation source, being focused on the sample's surface by 20 $\times$  objective (NA =  
192 0.25). The Raman peak position was corrected using the reference mode of Si at 521  
193  $\text{cm}^{-1}$ . Ag concentration in the studied solutions was determined by using an ICP OES  
194 iCAP 6300 Duo device (Thermo Fisher Scientific, Bremen, Germany), with an axial  
195 and radial view, simultaneous detector CID (Charge Injection Device). Commercial  
196 purity argon 99,996% (White Martins-Praxair) was used to purge the optics, plasma  
197 generation, and nebulizer and auxiliary gas. All determinations by ICP OES were carried  
198 out in plasma axial view under the following operational conditions: 1150 W RF power,  
199 12  $\text{L}\cdot\text{min}^{-1}$  plasma gas flow rate, 0.50  $\text{L}\cdot\text{m}^{-1}$  nebulizer gas flow, 50 rpm analysis pump  
200 rate, 15 s integration time. The Ag 328.068 nm emission line was used in all ICP OES  
201 determinations. The linear dynamic range was between 0.20 – 5.00  $\text{mg}\cdot\text{L}^{-1}$ , with  $R^2 =$   
202 0.9997. The limit of detection (LOD), calculated according to IUPAC's

203 recommendations (3 times the standard deviation of the blank (Sbl, n = 10) divided by  
 204 the calibration curve slope (m)), was 0.002 mg L<sup>-1</sup> of Ag with a limit of quantification  
 205 (LOQ = 10\*Sbl/m) of 0.006. Ag<sup>+</sup> ions liberation from the AgNPs, in distilled water, was  
 206 also determined by dialysis experiments [41,42], using dialysis tubing with a molecular  
 207 weight cut-off at 12,000 Da – with an approximate exclusion diameter of 2.5 nm –  
 208 (Sigma-Aldrich). 5 mL of nanomaterial solution (AgNPs or AgNPs/r-GO<sub>#1</sub> or AgNPs/r-  
 209 GO<sub>#2</sub>) containing 500 mg L<sup>-1</sup> of AgNPs filled the dialysis tubing; then, it was placed in  
 210 a beaker containing 45 mL of distilled water, totaling 50 mL. The silver concentration  
 211 in the filtrate solution was determined by collecting 5 mL of water from the beaker after  
 212 48 h and determining the Ag content in a Thermo iCAP 6300 Duo ICP OES (Thermo  
 213 Fisher Scientific). The Ag<sup>+</sup> concentration was determined considering the Ag content  
 214 before ultrafiltration. The rate constant of dissolution (K<sub>d</sub>) was determined by using the  
 215 dissolution curve model presented in Eq. 1, which is based in a first order kinetics model  
 216 and usually used to obtain the Ag dissolution (Ag<sup>+</sup> ions liberation) rate constant (K<sub>d</sub><sup>Ag<sup>+</sup></sup>)  
 217 [43–45].

$$218 \quad [A_g^+]_t = [A_gNPs]_o (1 - e^{-(K_d^{Ag^+})t}) \quad (1)$$

219  
 220 where [A<sub>g</sub><sup>+</sup>]<sub>t</sub> represents the concentration of Ag<sup>+</sup> ions liberation at some point in time (t), after  
 221 dissolution has started at an initial concentration of silver nanoparticles of [A<sub>g</sub>NPs]<sub>o</sub>. The  
 222 determination of the reactive oxygen species (ROS) produced by the Ag-containing samples  
 223 under blue-light irradiation was performed using a non-fluorescent marker, the 2',7'  
 224 *Dichlorofluorescein diacetate* (DCFH-DA) (*Sigma Aldrich*), which is oxidized by interacting  
 225 with ROS, forming a highly fluorescent molecule (DCF) [46,47]. Initially, a DCFH-DA stock  
 226 solution was prepared in ethanol (5 mM). The DCFH-DA and Ag-containing sample were

227 placed in a quartz cuvette by diluting in distilled water to obtain a final solution containing a  
228 concentration of 0.34 mM and 1.5 mg L<sup>-1</sup> of DCFH-DA and Ag, respectively. Then, the ROS  
229 production was determined in real-time by exciting the samples at 470 nm and collecting the  
230 emission between 500 and 600 nm. The first 10 min of ROS production was monitored in dark  
231 conditions (chemical reaction), and then blue-light was turned on to determine ROS production  
232 under illumination (photochemical reaction), as represented in Fig. S1 of the supplementary  
233 materials. The same procedure was carried out with the control groups by testing the GO,  
234 coffee and distilled water (H<sub>2</sub>O - negative control). Finally, the rate constant of ROS production  
235 ( $k_{ROS}$ ) was estimated by using Eq. 2 as explained in detail in the supplementary material.

$$236 \quad -\frac{d[ROS]}{dt} = k_{ROS} [DCFH : DA][ROS] \quad (2)$$

237

238 **2.6. Bactericidal assay.** The experiments were performed using *Staphylococcus aureus*  
239 strain ATCC 25923. The strain was maintained at -70 °C in Brain Heart Infusion (BHI)  
240 containing glycerol (20% v/v). For bacterial suspension preparation, 40 μL of the  
241 bacterial strain was added in 4 mL of BHI and kept in an oven at 37 °C for 24h. After  
242 that, the bacterial solution was prepared to achieve the turbidity standard of 1.0 Mc  
243 Farland. Then, 500 μL of the tested materials (AgNPs, GO, AgNPs/r-GO<sub>#1</sub>, and  
244 AgNPs/r-GO<sub>#2</sub>) were diluted in 500 μL of a saline solution containing the bacterial  
245 inoculum. Two control groups were also tested by using the coffee solution and distilled  
246 water (H<sub>2</sub>O - negative control) in which 500 μL of control solution (coffee or H<sub>2</sub>O) was  
247 added in 500 μL of a saline solution containing the bacterial inoculum. Consequently,  
248 for all prepared samples the final concentration of bacterial solution achieved the  
249 turbidity standard of 0.5 Mc Farland (1.5 x 10<sup>8</sup> UFC.mL<sup>-1</sup>).

250 The bactericidal assay was performed by adding the prepared sample solutions in an  
251 incubator at 37 °C and collecting aliquots after 0.5, 1.0, 3.0, and 6.0 h for testing the  
252 antibacterial activity of the samples as a function of the time. For this purpose, 200 µL  
253 of each sample was collected and placed into a 96-well microplate; then a serial dilution  
254 was performed until a dilution of 1:32. The total bacteria number was determined by the  
255 spread plate method, using the Plate Count Agar (PCA) medium (Acumedia, Neogen,  
256 Lansing, Michigan, USA) in which the colony-forming units (CFU) were counted 18 h  
257 after the incubation at 37 °C.

258

259 **2.7. Photobactericidal assay.** The photobactericidal assay was carried out also using *S.*  
260 *aureus* strain ATCC 25923 in which the strain was maintained at -70 °C in Müller  
261 Hinton Broth containing glycerol (20% v/v). For bacterial suspension preparation, 40  
262 µL of the bacterial strain was added in 4 mL of Brain Heart Infusion broth (BHI) and  
263 kept in an oven at 37 °C for 24 h. Then, bacterial concentration was prepared to achieve  
264 the turbidity standard 0.5 Mc Farland. After that, the investigated solution (H<sub>2</sub>O, Coffee,  
265 AgNPs, GO, AgNPs/r-GO<sub>#1</sub>, and AgNPs/r-GO<sub>#2</sub>) was diluted in 2 mL of a saline  
266 solution containing the bacterial inoculum. The tested concentrations were 0.0 (negative  
267 control), 50 ppm of Ag (AgNPs, AgNPs/r-GO<sub>#1</sub>, and AgNPs/r-GO<sub>#2</sub>), and 0.23 ppm for  
268 GO (the GO concentration in the AgNPs/r-GO<sub>#1</sub>, and AgNPs/r-GO<sub>#2</sub> samples). After the  
269 addition of tested solutions, the samples were placed in a shaker and agitated at 120 rpm  
270 over 30 min. After the solutions incubation, the samples were separated into two groups:  
271 one submitted to blue light irradiation (irradiated group) and another kept in the dark  
272 (dark control group). 200 µL of each irradiated sample was placed in a 96-well and then  
273 illuminated by using a homemade LED device (UFGD, Dourados, MS, Brazil) as a light  
274 source. The samples were irradiated at 450 nm with a light intensity of 9.5 mW.cm<sup>-2</sup>

275 during 30, 45, and 90 min, corresponding to energy doses of 17.1, 25.7, and 51.3 J.cm<sup>-</sup>  
276 <sup>2</sup>, respectively. Here it is important to stress that a low light intensity of 9.5 mW.cm<sup>-2</sup>  
277 was designed in the present experimental setup to avoid heating the samples  
278 (photothermal effect) during the irradiation process. Finally, the samples of both groups  
279 (irradiated and non-irradiated) were submitted to a serial dilution until a dilution of 1:32.  
280 The total bacteria number was determined by the spread plate method using the Plate  
281 Count Agar (PCA) medium, and then the colony-forming units (CFU) were counted 18  
282 h after the incubation at 37 °C. All measurements were performed in triplicate, and the  
283 statistical analyses were performed, considering the adopted repetitions, and addressing  
284 the CFU values obtained for the three light doses and dark control groups.

285

## 286 **2.8. Morphological evaluation of bacteria by scanning electron microscopy.**

287 Morphology and interaction of bacteria with the nanomaterials were investigated in a  
288 scanning electron microscope (SEM, JEOL model JSM-6380LV). The experiments  
289 were performed in the irradiated and non-irradiated AgNPs/GO composites containing  
290 bacteria, as well as in the control samples (bacteria/water and bacteria/coffee only). All  
291 experiments were prepared by dispersing the sample immediately after finishing the  
292 bactericidal or photobactericidal assays (approx. 200 µL) into an Eppendorf containing  
293 200 µL of a phosphate buffer solution (PBS) at pH 7.0. Then, the samples were  
294 centrifuged several times at 3000 rpm for 5 minutes, discarding the supernatant. The  
295 centrifugations were performed in PBS (three times), ethanol 70%, 80%, 90%, and  
296 absolute ethanol, in this order. Finally, the precipitate was dispersed in absolute ethanol  
297 and stored in the refrigerator. Pieces of glass coverslip (1 x 1 cm) were cut and cleaned  
298 in water/soup, ethanol and acetone for 20 minutes each process, using a sonicator. The  
299 glass substrates were painted with glutaraldehyde and held at ambient conditions

300 overnight for drying to further fix the bacteria/nanocomposites. After depositing onto  
301 the glass surface, samples were coated with a thin gold layer using the sputter coater and  
302 attached to the SEM sample holders by using conductive carbon tape. Images were taken  
303 at the following conditions: 10 kV, spot size 10, and a working distance of 8 mm.

304

305 **2.9. DNA extraction and PCR amplification.** DNA was extracted from 150  $\mu$ L *S.*  
306 *aureus* cells using the CTAB method as previously described [48]. PCR amplification  
307 of a putative transcriptional regulator gene of *Staphylococcus aureus* was performed  
308 using the primers Sa0836F (5'-GGCGCTTGTAATAATTTTCGT-3') and Sa0836R (5'-  
309 TGCGCAAAGTTTTATTGAACA-3') and the cycling conditions as previously  
310 described [49]. PCR amplification was performed in 25  $\mu$ L reactions using a ABI Verity  
311 Thermal Cycler (ThermoFisher) for 35 cycles. The reaction mixture consisted of  
312 appTAQ RedMix (Appleton Woods Limited, UK), 400 nM of forward and reverse  
313 primers and ~100 ng of template DNA. Reaction mixtures with no template DNA were  
314 used as a negative control.

315

316 **2.10. Endogenous photosensitizer extraction and identification.** The bacterial extract  
317 was obtained by performing the following steps, adapted from Mancini and Imlay  
318 (2015) [50]: (i) 100 mL of bacterial cell suspension with an absorbance of 0.4 at 600 nm  
319 (A<sub>600</sub>) was prepared; (ii) The bacterial cell suspension was centrifuged at 7000g at 4  
320 °C during 10 min; (iii) Bacterial cells in the pellet was washed in 20 mL pre-chilled PBS  
321 and then resuspended in 10 mL of the same buffer; (iv) The resuspended solution was  
322 adjusted, by adding PBS, to reach again an A<sub>600</sub> of 0.4 and, then, centrifuged at 7000g  
323 at 4 °C for 10 min; (v) The cell pellet was resuspended in 1 mL of ethyl acetate/acetic  
324 acid (3:1, v/v); (vi) The cells were lysed by sonication for 2 min on ice; (vii) Finally,

325 the cell debris was removed by centrifuging at 7000g at 4 °C for 10 min and then  
326 collecting the supernatant. The obtained fluorescence spectrum of the bacterial extract  
327 was determined and compared with the corresponding spectra of the protoporphyrin IX  
328 and riboflavin, standard compounds purchased from Sigma-Aldrich that represent the  
329 optical feature of porphyrins and flavins, respectively. The fluorescence spectra were  
330 collected in the 500 to 750 nm range when excited at 450 nm with aid of a Shimadzu-  
331 RF-6000 spectrofluorometer and using a quartz cuvette with four polished faces and an  
332 optical path length of 1 cm.

333

### 334 **3. RESULTS AND DISCUSSION**

#### 335 **3.1. AgNPs, GO and AgNPs/r-GO preparation and characterization**

336 Fig. S2 of Supplementary Information shows SEM and TEM images of GO obtained in  
337 this work. It is observed the formation of a two-dimensional material in the form of  
338 individual sheets with micrometric dimensions, in agreement with previous results in  
339 the literature [31,51,52]. Nevertheless, sheets with lateral sizes ranging from 4 to 700  
340  $\mu\text{m}$  were observed, reveling a broad size distribution as can be seen in the histogram  
341 presented in Fig. S2c. Fig. S2d shows the Raman spectrum of the GO sample contains  
342 two main peaks centered at 1353 and 1598  $\text{cm}^{-1}$ , which are attributed to D and G bands,  
343 respectively[53–55]. The intensity ratio of these two vibrational bands ( $I_D/I_G$ ) is  
344 commonly used to distinguish the formation of GO and r-GO. The obtained intensity  
345 ratio  $I_D/I_G = 1.03$  is an assignment of GO formation [56]. After the preparation of the  
346 AgNPs in the presence of GO by using the coffee extract solution as reducing agent, D  
347 and G bands shifted to approx. 1330 and 1597  $\text{cm}^{-1}$  for the composite #1 and 1335 and  
348 1594  $\text{cm}^{-1}$  for the composite #2 (Fig. S3), respectively. In addition, the intensity ratio  
349  $I_D/I_G$  increased to 1.13 and 1.09 for the composites #1 and #2, respectively, which

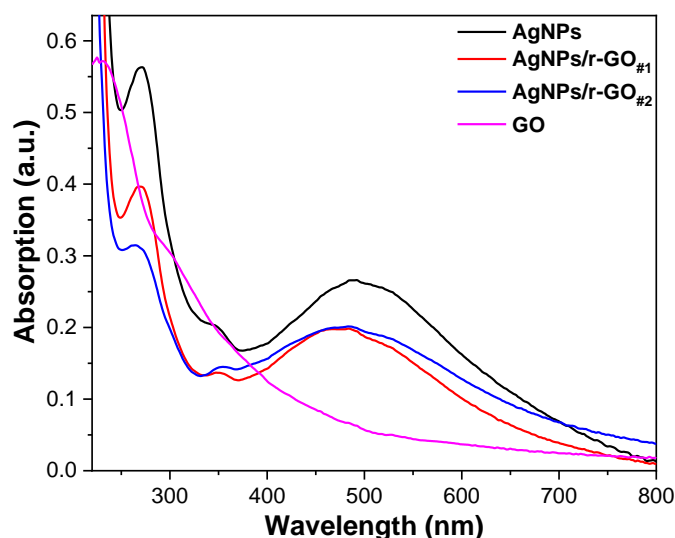
350 represents an increased degree of disorder. The higher  $I_D/I_G$  intensity ratio indicates the  
351 GO chemical reduction[56,57]. Therefore, GO suffered reduction to r-GO during  
352 AgNPs decoration and the composites hereafter are called AgNPs/r-GO. Furthermore,  
353 the additional vibrational bands at 242, 816, 945, 1037, 1287, 1375 and 1586  $\text{cm}^{-1}$  are  
354 ascribed to the surface-enhanced Raman scattering (SERS) by organic molecules  
355 present in the coffee solution adsorbed at the surface of AgNPs [58–61]. For instance,  
356 the bands at 1287 and 1375  $\text{cm}^{-1}$  are originated from the C–N stretching vibrations with  
357 contributions from ring bending and ring C–H bending vibrations; the peaks at 1586 and  
358 1030  $\text{cm}^{-1}$  are attributed to the ring C–C and C–H (with contributions from C–O)  
359 stretching vibrational modes[60–62], respectively; and the vibrations at 816 and 945  $\text{cm}^{-1}$   
360 are probably due to the presence of carotenoids [59–61,63]. Finally, the vibrational  
361 band at 544  $\text{cm}^{-1}$  arises from the Si substrate.

362 It is worth noting that r-GO is usually obtained by using highly toxic and hazardous  
363 chemicals such as hydrazine, di-methylhydrazine, hydroquinone, sodium borohydride,  
364 etc., which introduce several harmful effects on the environment and human health even  
365 at trace amounts. Consequently, by-products from the toxic reducing agents may be left  
366 behind during the synthesis process, can cause adverse effects and have to be avoided  
367 during a medical application or treatment. Therefore, our results show that the coffee  
368 extract acts as a green reducing agent for both silver nitrate and GO, resulting in the  
369 environmentally friendly production of AgNPs/r-GO composites in a simple and non-  
370 toxic reaction set-up with a satisfactory yield. In fact, the reduction of GO by aqueous  
371 phytoextracts has been reported before and a mechanism for the reduction has been  
372 proposed [64]. As it was also observed for other phytochemicals [65,66], the coffee  
373 extract contains phenolic compounds that are easy to get oxidized, which presented  
374 sufficient potential to reduce the oxygen-containing groups of GO as well as  $\text{Ag}^+$  ions.

375 During the synthesis, reduced silver atoms can interact by physisorption or electrostatic  
376 binding [67] with the functional groups present in the high surface area of the GO which  
377 function as nucleation sites for NPs' growth and stabilization [68], with several  
378 advantages such as avoiding aggregation and facilitating their recovery from the  
379 environment by sedimentation [69–72]. Therefore, the presented green method takes  
380 benefit from the GO surface as a suitable platform for the deposition of silver ions to  
381 form metal nanoparticle composites for bio-related applications using coffee extract as  
382 a green reductant.

383 The prepared samples presented different colors by naked eye observation, ranging  
384 from transparent brown (coffee extract) to opaque dark brown (AgNPs) and brownish-  
385 green (AgNPs/r-GO composites), as can be seen in Fig. S4b of supplementary materials.  
386 The UV-Vis absorption spectra of AgNPs and AgNPs/r-GO composites revealed a  
387 broad absorption band in the 400 to 700 nm, as presented in Fig. 1. It is well-known that  
388 colloidal AgNPs have a characteristic optical absorption band with maximum in the 450  
389 - 490 nm range as a result of the SPR, phenomenon induced by the collective electron  
390 oscillations at the metal nanoparticle surface [7,8], which can be used to monitor NPs  
391 formation as only nanostructured materials present surface Plasmon resonance [73]. Fig.  
392 1 also shows that the GO spectrum presented a characteristic absorption peak at around  
393 230 nm due to the  $\pi$ - $\pi^*$  electronic transitions of the C-C aromatic bonds and a shoulder  
394 at around 300 nm that can be attributed to n- $\pi^*$  transitions of C=O bond bands [74].  
395 AgNPs sample showed an absorption peak centered at ~490 nm which is assigned to the  
396 SPR of AgNPs [4,14,15,75,76]. An additional peak at 270 nm can be seen in the UV-  
397 Vis absorption spectrum of AgNPs which was previously attributed to caffeine [77,78].  
398 In addition to the caffeine absorption band, a small absorption shoulder appeared at 350  
399 nm for all coffee-extract-containing samples that may be attributed to Chlorogenic acids

400 (CGAs) [79]. The presence of caffeine and CGAs in the pure coffee extract used in this  
401 work was further confirmed by HPLC (Fig. S4a). A comparison of the UV-Vis  
402 absorption spectrum for pure coffee extract and AgNPs can be seen in Supplementary  
403 Material (Fig. S5). It is worthy of noting that the SPR peak observed in the spectrum of  
404 the AgNPs sample seems to be quite broad, but in fact, this is a result of the overlapping  
405 of two distinct contributions, one coming from the broad absorption band of the coffee  
406 extract solution with a maximum at 455 nm, and the other from the SPR of AgNPs with  
407 a maximum absorption at 490 nm (see Fig. S5 of supporting information). For both  
408 AgNPs/r-GO composites, the SPR band originated from the collective electron  
409 oscillations at the AgNPs surface was ~15 nm blue-shifted when compared to the pure  
410 AgNPs, presenting the absorption bands centered at around 475 nm. In addition, the  
411 SPR absorption intensities of the AgNPs/r-GO composites were lower than the free  
412 AgNPs absorption, indicating a reduction of the total surface area available for the  
413 collective oscillations of the electrons at the AgNPs surface of the composites as a result  
414 of the adsorption of the AgNPs on the r-GO surface (i.e., the surface part of the AgNPs  
415 in contact with the r-GO surface is not available for the electron oscillation, reducing  
416 the total surface area for the occurrence of SPR). Nevertheless, reduction of the SPR  
417 absorption related to a size increase of the formed particle and/or a concentration  
418 decrease of the AgNPs produced in the presence of the r-GO should not be ruled out and  
419 it will be further discussed.



420

421 **Figure 1** - UV-Vis absorption spectra of GO, AgNPs, AgNPs/r-GO<sub>#1</sub>, and AgNPs/r-GO<sub>#2</sub>.

422

423 ICP OES analysis was performed to determine the Ag concentration in the colloidal  
 424 AgNPs and AgNPs/r-GO composites. The obtained Ag concentration was approx. 1256,  
 425 1154 and 1161 mg.L<sup>-1</sup> for AgNPs, AgNPs/r-GO<sub>#1</sub> and AgNPs/r-GO<sub>#2</sub>, respectively, as  
 426 presented in Table S1. The lower concentration of Ag observed for the composites when  
 427 compared to the free AgNPs was due to the fact that the reaction volume was increased  
 428 during the synthesis of the composite, once 2 mL of GO aqueous solution was  
 429 introduced in 12 mL of AgNPs for obtaining 14 mL of the AgNPs decorated GO sheets  
 430 solution. Therefore, it should be expected a reduction of around 16% in the  
 431 concentration of silver in the colloidal solution of the AgNPs/r-GO composites.  
 432 However, the ICP results show that this difference is only about 9%, indicating that the  
 433 synthesis yield of Ag ions reduction was higher when in the presence of the GO sheets.  
 434 Even though, it is worth pointing out that this reduction of 9% in the AgNPs  
 435 concentration observed in the AgNPs/r-GO composites cannot alone explain the  
 436 reduction of 30% observed by the SPR absorption measurements, reinforcing that part  
 437 of the absorption decrease is a consequence of the adsorption of the AgNPs on the r-GO

438 surface (i.e., the reduction of the total surface area available for the collective  
439 oscillations of the electrons at the AgNPs surface).

440 The morphology of the AgNPs and the AgNPs/r-GO composites were investigated  
441 by FEG-TEM, as presented in Fig. 2. For AgNPs (Fig. 2a), it is possible to see the  
442 formation of nanoparticles with irregular shapes and a mean size of about  $77 \pm 36$  nm,  
443 which represents a relatively broad size distribution. Figs. 2b and 2c show that even  
444 some isolated nanoparticles could be observed, the AgNPs were preferentially deposited  
445 over the r-GO sheets for the AgNPs/r-GO composites. These results confirm the  
446 existence of an intrinsic contact between AgNPs and r-GO sheets. It is important to  
447 stress that AgNPs produced in both AgNPs/r-GO composites presented similar  
448 morphological and size characteristics that include irregular-shaped particles and could  
449 not be distinguished by TEM observations. The AgNPs obtained for the AgNPs/r-GO<sub>#1</sub>  
450 presented a mean size of  $70 \pm 12$  nm. For AgNPs/r-GO<sub>#2</sub>, a very similar size and size  
451 distribution could be found, with mean a value of  $65 \pm 11$  nm. This result shows that no  
452 matter the order chosen for the chemical synthesis driven deposition of the AgNPs over  
453 the r-GO surface, the size and shape of the obtained NPs are almost identical. In  
454 addition, the Ag<sup>+</sup> ions liberation results demonstrated that all Ag-containing samples  
455 (AgNPs, AgNPs/r-GO<sub>#1</sub> and AgNPs/r-GO<sub>#2</sub>) presented similar Ag<sup>+</sup> release rate as shown  
456 in Table 1. A concentration of  $35.9 \pm 1.5$ ,  $34.5 \pm 1.2$ , and  $35.6 \pm 2.0$  mg L<sup>-1</sup> was determined  
457 for the Ag<sup>+</sup> released by AgNPs, AgNPs/r-GO<sub>#1</sub> and AgNPs/r-GO<sub>#2</sub>, respectively, when  
458 Ag-containing samples were kept during 48h in an aqueous solution. Consequently, a  
459 rate coefficient of Ag<sup>+</sup> release ( $K_d^{Ag^+}$ ) of  $0.027 \pm 0.001$ ,  $0.025 \pm 0.001$ , and  $0.026 \pm 0.002$  h<sup>-1</sup>  
460 <sup>1</sup> was determined for the AgNPs, AgNPs/r-GO<sub>#1</sub> and AgNPs/r-GO<sub>#2</sub>, respectively. The

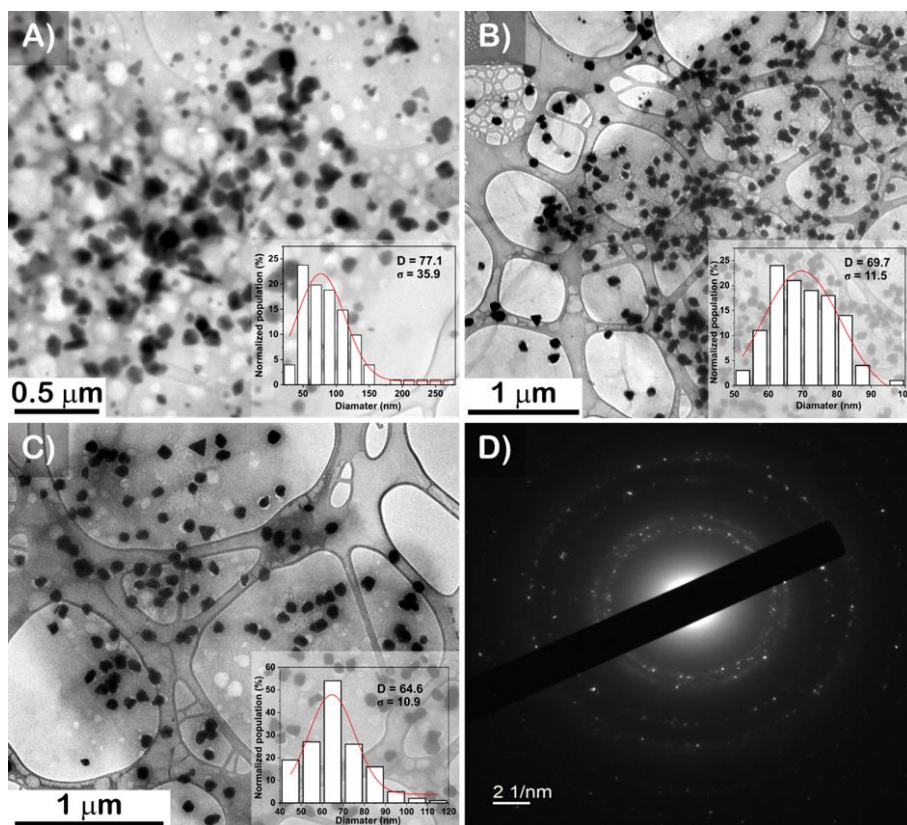
461  $K_d^{Ag^+}$  determination was based in the first-order kinetics model [43] of Eq. 1, which is  
 462 presented in more detail in the supplementary materials.

463 Fig. 2d shows a representative selected area electron diffraction (SAED) obtained for  
 464 the AgNPs/r-GO<sub>#1</sub> composite. As a result, diffraction rings with diameters of 2.22, 1.96,  
 465 1.38 and 1.17 Å were obtained, which are very close to the interplanar spacing of (111),  
 466 (200), (202) and (222) planes of the cubic crystalline phase of silver, space group F m -  
 467 3 m and cell parameter equal to 4.126 Å (COD entry 9013048). Similar results were  
 468 obtained for AgNPs and AgNPs/r-GO<sub>#2</sub> composite (not shown) which confirms the  
 469 presence of face-centered cubic crystalline silver for all synthesized samples.

470 **Table 1** – Diameter of Ag nanoparticles determined by TEM, hydrodynamic diameter of Ag-containing samples  
 471 obtained by DLS, Zeta potential (Zp) in aqueous solution, and rate coefficient of Ag<sup>+</sup> release ( $K_d^{Ag^+}$ ), respectively.

Sample	AgNPs diameter (nm)	Hydrodynamic diameter (nm)	Zp (mV)	$K_d^{Ag^+}$ (h <sup>-1</sup> )
AgNPs	77±36	138 ± 73	- 11.2 ± 6.9	0.027±0.001
AgNPs/r-GO <sub>#1</sub>	70±12	> 1000	- 25.3 ± 7.2	0.025±0.001
AgNPs/r- GO <sub>#2</sub>	65±11	> 1000	- 22.3 ± 6.2	0.026±0.002

472



473

474 **Figure 2** – TEM images of the synthesized (a) AgNPs, (b) AgNPs/r-GO#1, and (c) AgNPs/r-GO#2.  
 475 Selected area electron diffraction image of the AgNPs/r-GO#1(d).

476

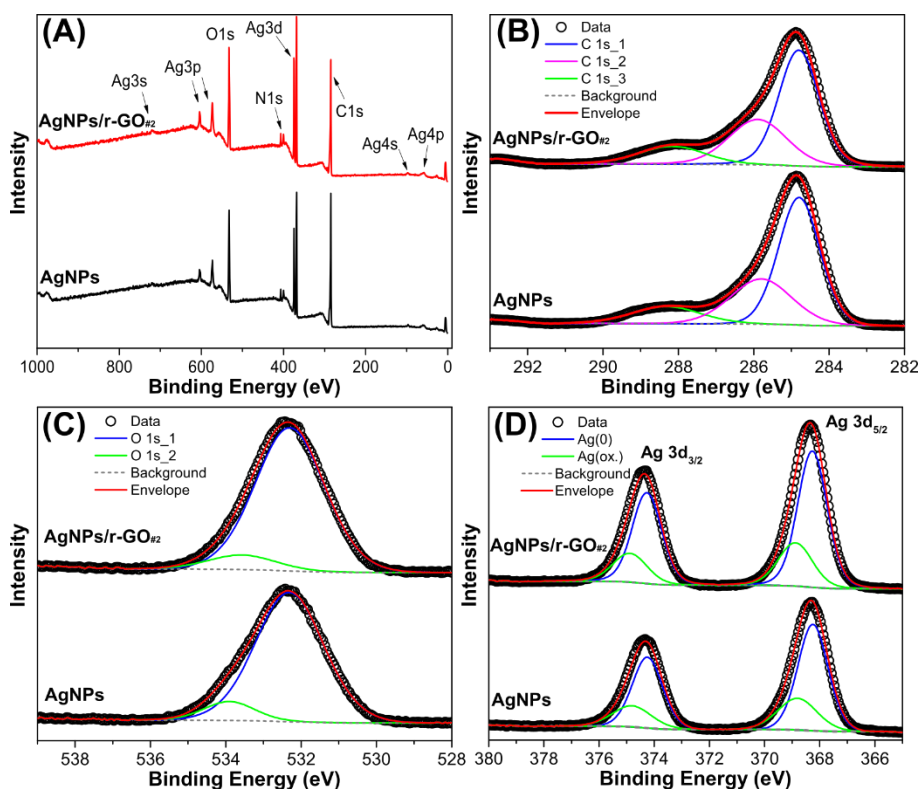
477 DLS (dynamic light scattering) experiments were also performed to determine the  
 478 hydrodynamic size of the particles as  $138 \pm 73$  nm, with monomodal size distribution  
 479 and a polydispersity index (PDI) of 0.246, indicating that the particles are nearly-  
 480 monodispersed. Herein, the size of the AgNPs obtained by DLS is bigger than that  
 481 obtained by TEM (Table 1), as expected, since it takes into account the functional groups  
 482 that potentially may attach to the surface of the nanoparticles [80]. DLS results for the  
 483 AgNPs/r-GO composites revealed the presence of micro-sized aggregates due to r-GO  
 484 presence and, therefore, it was not possible to determine with precision the exact size of  
 485 the AgNPs in the composites.

486 Zeta potential measurements were applied to study the surface charge of the AgNPs  
 487 and the AgNPs/r-GO composites. Considering only the coffee extract solution the

488 obtained Zeta potential was  $-27.6 \pm 5.5$  mV. When the AgNPs were synthesized in the  
489 coffee extract solution, the Zeta potential negatively decreased to  $-11.2 \pm 6.9$  mV,  
490 indicating that the AgNPs may contribute with a positive or less negative surface charge  
491 for the colloidal solution. However, the Zeta potential value negatively increased to  $-$   
492  $25.3 \pm 7.2$  mV and  $-22.3 \pm 6.2$  mV for the AgNPs/r-GO<sub>#1</sub> and AgNPs/r-GO<sub>#2</sub>  
493 composites, respectively, revealing different surface charge properties when compared  
494 with the free AgNPs.

495 Fig. 3 shows XPS results for AgNPs and a representative AgNPs/r-GO<sub>#2</sub> composite.  
496 The survey spectrum showed in Fig. 3a confirms that no other elements are present in  
497 the surface composition of samples rather than C, O, N, and Ag. It is important to note  
498 that the N contribution comes from the coffee. Survey spectra were used for the  
499 quantification of the sample surface chemical composition (see Table S2). The high-  
500 resolution C 1s spectra presented a main peak that was attributed to adventitious carbon  
501 (C-C sp<sup>2</sup>) and used to calibrate the energy at 284.8 eV. Fig. 3b shows high-resolution  
502 spectra of C 1s regions, where three peaks centred at 284.8 eV, 285.90 eV and 288.05  
503 eV were detected and assigned to the C-C, C=C (284.8 eV), C-O, C=O (285.9 eV) and  
504 O-C=O (288.1 eV) bonds [54,55,81–83]. It is important to highlight that the C 1s XPS  
505 spectra of AgNPs and AgNPs/r-GO<sub>#2</sub> are almost identical and could not be used to  
506 distinguish GO contribution. Fig. 3c presents the O 1s spectra which contains two peaks;  
507 one main contribution at 532.3 eV that is attributed to O-(C=O<sup>\*</sup>)-C (aliphatic), and the  
508 other located at 533.9 eV that may be attributed to C-OH in an aromatic environment  
509 [84]. In addition, Ag 3d spectra of the free AgNPs and AgNPs/r-GO<sub>#2</sub> samples were  
510 very similar, presenting two peaks centred at 368.3 and 374.3 eV that corresponds to Ag  
511 3d<sub>5/2</sub> and Ag 3d<sub>3/2</sub>, respectively, as shown in Fig. 3d. For the fitting components, the  
512 spin-orbit doublet energy separation and area ratio was set at 6.0 eV and 2:3,

513 respectively, and the full-width at half maximum (fwhm) values were constrained to  
 514 coincide for the same doublets and restrained to values between 1 and 2. Moreover, for  
 515 the correct fitting of these spectra, two contributions had to be taken into account (green  
 516 and blue lines in Fig. 3c), one with an Ag 3d<sub>5/2</sub> peak located at 368.3 eV, corresponding  
 517 to metallic silver, and other with an Ag 3d<sub>5/2</sub> peak located at 368.8 eV, assigned to  
 518 oxidized silver [85]. All peak position values and atomic percentages obtained by the  
 519 XPS analysis can be seen in Table S2.



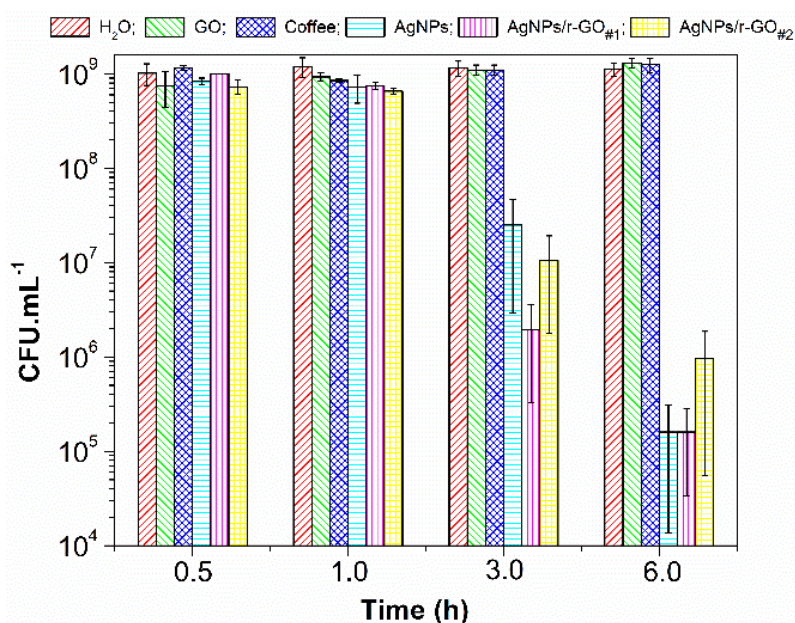
520  
 521 **Figure 3** - XPS spectra of the AgNPs and AgNPs/GO<sub>#2</sub> samples: a) Survey; b) C 1s; c) O 1s and d) Ag  
 522 3d regions.

523  
 524 **3.2. Antibacterial activity.** The antibacterial activities of the tested samples against *S. aureus*  
 525 are presented in Fig. 4. The results revealed that GO sheets were not able to avoid the bacterial  
 526 growth during 6 h of interaction with the bacteria, presenting a similar response observed for  
 527 water and coffee extract samples (control solutions) as can be seen in Fig. S6 in the  
 528 supplementary materials. Therefore, our results indicate that the prepared GO sheets were not

529 able to induce physical damage to the bacterial cell walls, which could promote the formation  
530 of pores in the cell walls and, consequently, cell death caused by an osmotic imbalance [86].  
531 This assumption was confirmed by SEM results which demonstrated that the bacterial cells  
532 remained intact after interacting with the GO sheets as presented in Figure S9 of the  
533 supplementary material. The SEM images indicate that the bacteria were wrapped by the GO  
534 sheets during the sample preparation procedure. However, it is important to note that the  
535 bacterial cell walls have preserved their original rounded shape as observed prior to the  
536 interaction with GO. Although recent works have shown that GO can present different  
537 mechanisms of action against bacteria, such as oxidative stress induction, protein dysfunction,  
538 and transcriptional arrest [87,88], the GO antibacterial activity is mainly due to its capacity to  
539 kill bacteria by destroying the cell membrane, acting as a “knife” [89,90]. This GO feature is  
540 due to the unique two-dimensional (2D) shape, presenting sharp corners and edge protrusions  
541 that can easily destroy the bacterial cell walls and membranes [89]. However, it is worth to  
542 stress that the cell damage induced by GO is not only shape-dependent but is also dependent  
543 on the size of the GO sheet (i.e., dependent on the sheet area). For instance, Perreault et al. [91]  
544 have demonstrated that the antimicrobial activity of GO surface coatings against *Escherichia*  
545 *coli* decreased 4-fold after 3h of interaction between GO and bacteria when GO sheet area  
546 increased from 0.01 to 0.65  $\mu\text{m}^2$ . Additionally, their results also revealed that GO sheets with  
547 area of 0.65  $\mu\text{m}^2$  presented similar results to the control group, i.e., the largest tested GO sheet  
548 did not show antibacterial activity[91]. Furthermore, Akhavan and Ghaderi [90] have shown  
549 that GO nanosheets were very effective in killing both Gram-positive and Gram-negative  
550 bacteria by damaging the cell membrane of the bacteria as a result of direct contact of the  
551 bacteria with the extremely sharp edges of the GO during 2h. In addition, they also observed  
552 that Gram-positive bacteria, *S. aureus*, was less resistant to the cell membrane damage caused  
553 by the nano-GO than Gram-negative bacteria, *E. coli*, due to the lacking the outer membrane

554 of Gram-positive bacteria when compared to Gram-negative [90]. Based on that, we believe  
 555 that the lack of bacterial toxicity of the GO sheets applied in the present study, even after 6h of  
 556 contact with bacteria, may be related to their size because the tested GO presents a much higher  
 557 sheet area ( $> 9 \mu\text{m}^2$ ).

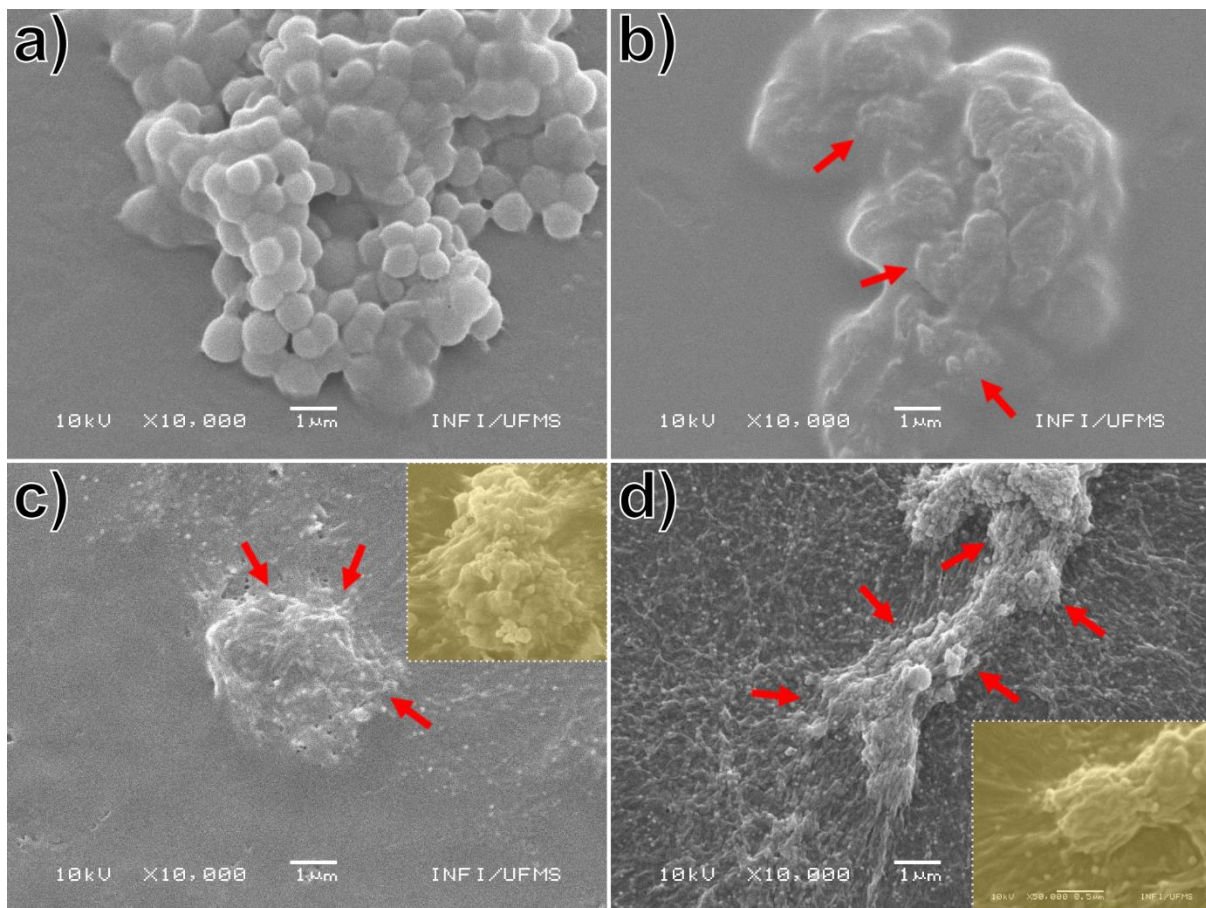
558 Nevertheless, it is important to stress that, in addition to their size, the antibacterial activity  
 559 of graphene family nanomaterials (GFNs) has been demonstrated to be also dependent on  
 560 oxygen content of the sheets [92], where more oxidative content can generate more ROS and,  
 561 consequently, can promote higher bactericidal effect. Hence, a low antimicrobial capacity  
 562 related to oxidative stress induction is expected from r-GO due to their low content of  
 563 functionalized oxygen-containing groups when compared with other graphene oxide  
 564 nanomaterials.



574 **Figure 4** - CFU mean values ( $\pm$ SD) of *S. aureus* after 0.5, 1.0, 3.0, and 6.0 h of interaction with Ag-free  
 575 (H<sub>2</sub>O, GO, Coffee) and Ag-containing (AgNPs, AgNPs/r-GO<sub>#1</sub>, and AgNPs/r-GO<sub>#2</sub>) samples.

577 Differently, free AgNPs and r-GO sheets decorated with AgNPs were very effective against  
 578 *S. aureus*. A reduction of approximately 2 logs in the bacterial count was promoted by AgNPs,  
 579 AgNPs/r-GO<sub>#1</sub>, and AgNPs/r-GO<sub>#2</sub> after 3h of interaction between the Ag-based

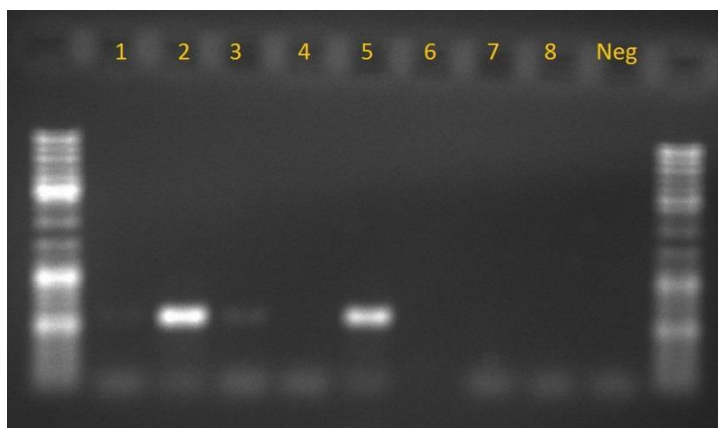
580 nanomaterials and bacteria. Although the obtained results presented in Fig. 4 possibly  
581 indicate an improvement trend of the antibacterial activity of the AgNPs/r-GO<sub>#1</sub>  
582 composite when compared with free AgNPs after 3h of interaction, no significant  
583 difference was observed after 6h in which all AgNPs-based materials induced a bacterial  
584 inhibition growth over 99.9% (*i.e.*, over 3 logs). The SEM results demonstrated that the  
585 antibacterial effect promoted by the Ag-containing nanomaterials was primarily due to  
586 a disruption of the integrity of the cell membranes as can be seen observed in Fig. 5.  
587



588 **Figure 5** - SEM images of *S. aureus* after 3.0 h of interaction with coffee extract (a), AgNPs (b), AgNPs/r-  
589 GO<sub>#1</sub> (c), and AgNPs/r-GO<sub>#2</sub> (d) samples. Red arrows indicate cell wall parts which are partially or  
590 completely damaged. Insets show AgNPs attached to the surface of the bacterial cells.

591

592 In addition, PCR amplification of the transcriptional regulation gene in *S. aureus*  
593 indicated that there was no DNA damage with *S. aureus* cells after 6 h of interaction in  
594 the dark with coffee (Lane 2), and GO (Lane 3) (Fig 6). However, DNA damage was  
595 observed with cells with AgNPs (Lane 4), and AgNPs/GO#2 (Lane 6).



596

597 **Figure 6** - Amplification of transcriptional regulation gene of *S. aureus*. Lanes (1) *S. aureus* – control; *S.*  
598 *aureus* after 6h of interaction with: (2) coffee, (3) GO, (4) AgNPs, (5) AgNPs/GO#1, and (6)  
599 AgNPs/GO#2; (7) *S. aureus* after 45 min of interaction with AgNPs under blue-light irradiation; (8) only  
600 *S. aureus* under blue-light illumination for 90 min; (Neg) PCR Control. GeneRuler DNA ladder  
601 (ThermoScientific).

602

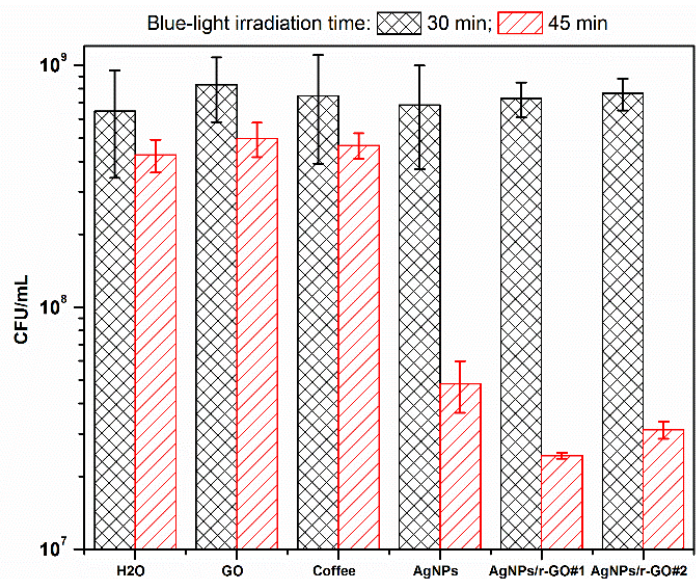
603 These results suggest that  $\text{Ag}^+$  liberation played a key role in bacterial toxicity as a  
604 similar  $\text{Ag}^+$  release percentage was determined for All AgNPs-based tested materials as  
605 shown in Table 1 and it is well established that the antibacterial activity of AgNPs is mainly  
606 due to the  $\text{Ag}^+$  liberation from nanoparticle surface [29,30]. Consequently, these results  
607 demonstrated that the AgNPs anchored on r-GO sheets may preserve their antibacterial  
608 properties. Prasad et al. [17] have reported a synergetic effect of AgNPs and r-GO  
609 against Gram-positive and Gram-negative bacteria, caused by the combined effect of  
610 the membranolytic and oxidative activity of r-GO with the free radical formation of  
611 AgNPs. They suggest that, in addition to the individual effects of the r-GO and AgNPs,

612 the synergic effect can be derived from the mechanical interaction between the sharp  
613 edges of r-GO sheets, which disrupts the cell membrane, and facilitates the transport of  
614 Ag<sup>+</sup> ions across the cell membrane [17]. Das et al. [93] have also demonstrated that the  
615 AgNPs/GO composites presented a considerable synergetic effect on membrane leakage  
616 of reducing sugars and proteins of Gram-positive bacteria. Against *S. aureus*, for instance,  
617 the synergetic effect of AgNPs/GO enhanced the sugar and protein leakage up to 65.15%  
618 and 137% after 8 h of incubation, respectively compared to GO nanosheets. When  
619 compared with AgNPs, they have shown that AgNPs/GO promoted an enhancement of  
620 32.93% and 27.95% of the sugar and protein leakage, respectively.[93] Differently to  
621 the previous studies, our prepared AgNPs/r-GO composites presented an antibacterial  
622 activity only due to the AgNPs toxicity against *S. aureus* as r-GO did not present  
623 antibacterial action and, consequently, no synergetic effect was observed. It should be  
624 noted that Liu et al. [67] have observed that the antibacterial activity AgNPs was  
625 enhanced when anchored on GO sheets, even when GO did not present any bactericidal  
626 effect. However, this observation was explained as a result of the avoiding of AgNPs  
627 aggregation promoted by the GO sheets, increasing the antibacterial activity of the  
628 nanoparticles due to the higher surface area to interact with bacteria [67]. Consequently,  
629 our results also indicated that the free AgNPs were well dispersed as similar inactivation  
630 was observed for all Ag-containing samples and no direct antimicrobial activity can be  
631 attributed to r-GO sheets as previously discussed.

632

633 **3.3. Photodynamic antibacterial activity.** The photobactericidal assays of the AgNPs-  
634 based materials were carried out by choosing an experimental set up to avoid the  
635 bactericidal activity (chemical effect) of AgNPs. As reported in the previous section, no  
636 antimicrobial effect was induced by Ag-based nanomaterials during the first hour. Based

637 on that, the photobactericidal experiments were carried out under blue light irradiation  
 638 by evaluating the antimicrobial photodynamic inactivation (aPDI) effect of the Ag-  
 639 containing nanomaterials on bacteria using a reduced concentration of AgNPs (10 times  
 640 lower than the used in the antibacterial activity, i.e., the presented in the previous  
 641 section) during up to 90 min of interaction. The aPDI of the tested samples against *S.*  
 642 *aureus* is presented in Fig. 7, revealing that no photoantibacterial activity was induced  
 643 by the Ag-based samples during the first 30 min of irradiation. However, a clear  
 644 bacterial photodynamic inactivation was observed for all Ag-based materials after 45  
 645 min of illumination, which was promoted exclusively by the AgNPs light absorption as  
 646 no bacterial inactivation was induced either for the control samples (coffee and GO  
 647 sheets) or for the light ( $H_2O$  sample) as presented in Fig. S7 in the supplementary  
 648 materials. These results also showed that, differently to the chemical effect, an  
 649 enhancement of the photoinactivation action was induced by AgNPs when anchored on  
 650 r-GO. Although small, a statistically significant reduction of bacterial growth was  
 651 determined, where the photoinactivation induced by AgNPs, AgNPs/GO<sub>#1</sub> and  
 652 AgNPs/GO<sub>#2</sub> achieved a bacterial growth reduction of 88.6, 94.3 and 92.7%,  
 653 respectively, as presented in Fig. 7.



654

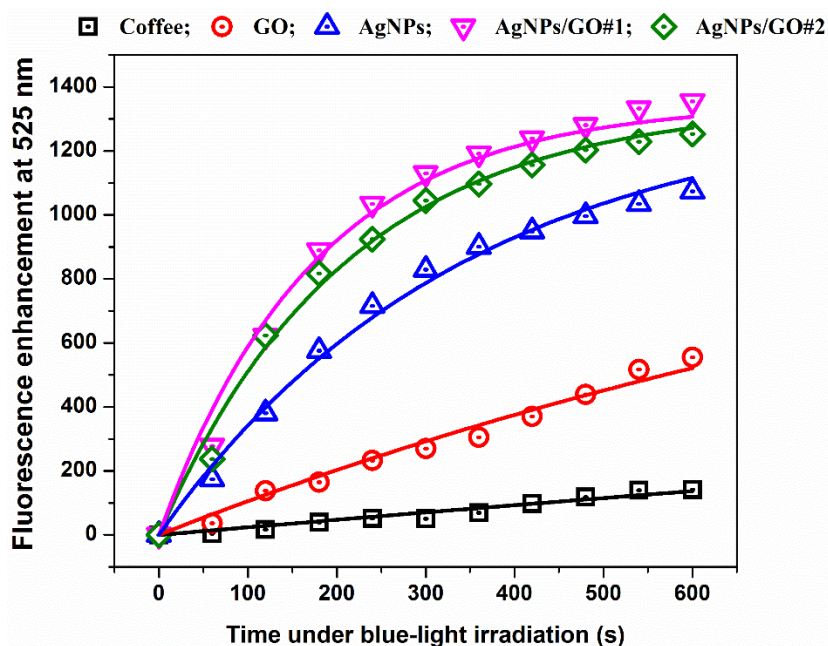
655 **Figure 7** - CFU mean values ( $\pm$ SD) of *S. aureus* after 30 and 45 min of interaction with Ag-free (H<sub>2</sub>O,  
656 GO, Coffee) and Ag-containing (AgNPs, AgNPs/r-GO<sub>#1</sub>, and AgNPs/r-GO<sub>#2</sub>) samples under blue light  
657 irradiation at 9.5 mW.cm<sup>-2</sup>.

658

659 The photodynamic effect induced by AgNPs shows that AgNPs acted as  
660 photosensitizers due to their SPR absorption band, where the Plasmon-excited states of  
661 AgNPs were able to transfer energy and/or charge (i.e., electron) to molecular oxygen  
662 located close to the NPs' surface, and then generating singlet oxygen by energy transfer  
663 and/or oxygen radicals by charge transfer (such as superoxide, hydrogen peroxide,  
664 hydroxyl radical), causing the bacterial death by oxidative stress induction [94,95].  
665 Recent investigations have proved that metal NPs, especially gold and silver NPs, can  
666 be efficient photosensitizers for photodynamic therapy because the photons can produce  
667 free electrons from the SPR during the light irradiation, which can promote the ROS  
668 production [95–97]. The synergetic effect observed for the AgNPs/r-GO composites can  
669 be explained by the enhancement of the oxidative stress induction promoted by an  
670 additional channel to generate oxygen radicals as the Plasmon-excited AgNPs may also  
671 transfer electrons to the surface of the r-GO, facilitating a long-range interfacial charge  
672 transfer process due to the good conductivity of the r-GO and, consequently, increasing  
673 the probability of ROS production because the photo-transferred electron can migrate  
674 to different parts of the r-GO sheet prior to finding an oxygen to react [38,40,98–100].  
675 Xie et al [38,101] have recently shown that the photocatalytic performance of AgNPs  
676 can be enhanced under 660 nm light irradiation once AgNPs bind to GO. They have  
677 demonstrated that the amount of ROS generation was increased because the excited-  
678 plasmon electrons can be rapidly transferred to the surface of GO sheets where ROS are  
679 generated, enhancing the photocatalytic activity of the AgNPs/GO composite due to the  
680 high conductivity of GO [38]. Although they showed that AgNPs/GO can promote a

681 rapid and efficient photoinactivation of *S. aureus*, killing almost all bacteria after 20 min  
682 of 660 nm red laser irradiation at 180 mW, this experimental irradiation setup also  
683 promoted an elevation of the temperature up to 42°C, which reflects that the  
684 photobactericidal activity of the AgNPs/GO was also influenced by a small  
685 photothermal effect. However, our findings reveal that AgNPs/r-GO composites can  
686 also exhibit a rapid and highly effective photodynamic antibacterial activity under a low  
687 dose of blue light irradiation (i.e., illuminating during 45 min at 9.5 mW.cm<sup>-2</sup>). Both  
688 AgNPs/r-GO composites caused a bacterial growth reduction greater than 92% after 45  
689 min of irradiation, exclusively due to the photodynamic action of AgNPs.

690 The capability of ROS generation by the Ag-based nanomaterials under blue-light  
691 irradiation is presented in Fig. 8, demonstrating the higher efficiency of ROS production  
692 by the AgNPs/r-GO composites. The apparent rate constant of ROS production ( $k_{ROS}$ )  
693 under blue-light illumination was obtained by using Eq. S5 to fitting the experimental  
694 results shown in Figure 8 (see details in the supplementary material). A  $k_{ROS}$  value of  
695 0.54±0.02, 2.43±0.07, 8.77±0.20, 17.18±0.71, and 14.26±0.43 was determined to  
696 coffee, GO, AgNPs, AgNPs/GO<sub>#1</sub>, and AgNPs/GO<sub>#2</sub>, respectively. These results are in  
697 accordance with the aPDI results, confirming the AgNPs/GO<sub>#1</sub> presents the highest  
698 photo-oxidative activity. Our findings also revealed that the photoantibacterial effect  
699 induced by the Ag-containing samples was mainly due to the bacterial cell membrane  
700 damage, as can be seen in Fig. S10 of the supplementary material [40,98–103]. The PCR  
701 results also revealed that AgNPs-containing sample promoted DNA damage in *S. aureus*  
702 cells after 45 min of interaction under blue-light irradiation (Lane 7) (Fig 6).



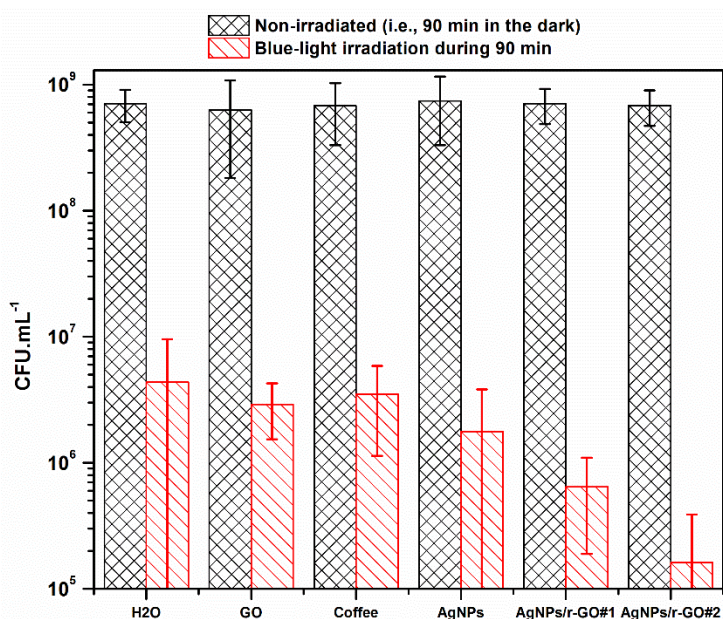
703

704 **Figure 8** - Fluorescence emission promoted by the ROS production under blue-light illumination as a  
 705 function of the time.

706

707 Although not statistically different, Fig. 7 also reveals a trend of reduction in the  
 708 bacterial growth for the Ag-free samples (H<sub>2</sub>O, GO, and coffee), possibly induced solely  
 709 by blue-light irradiation as similar results were obtained for the three samples. In fact,  
 710 several studies have demonstrated that *S. aureus* strains are susceptible to be  
 711 photoinactivated directly by blue-light due to photo-excitation of endogenous  
 712 intracellular molecules, which act as endogenous photosensitizers under blue-light  
 713 irradiation [104–106]. Our results also confirmed that *S. aureus* can be directly  
 714 photoinactivated by the blue-light irradiation under our experimental setup when  
 715 exposed to a higher dose of irradiation (Fig. S8a). A bacterial growth reduction of ~ 99.4  
 716 % (higher than 2 logs) was observed for the H<sub>2</sub>O, GO, and coffee samples under 51.3  
 717 J.cm<sup>-2</sup> as presented in Fig. 9. However, it is important to stress that Fig. 9 also shows  
 718 that AgNPs/r-GO composites induced a bacterial growth reduction greater than 3 logs  
 719 (higher than 99.9 %), revealing the combined effect promoted by the photobactericidal

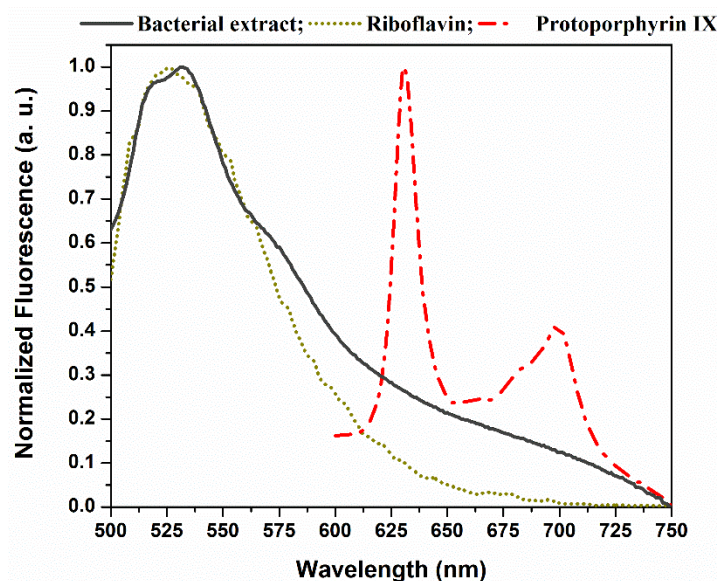
720 effect of blue-light irradiation and the photodynamic action caused by AgNPs/r-GO  
721 composites.



722  
723 **Figure 9** - CFU mean values ( $\pm$ SD) of *S. aureus* after 90 min of interaction with Ag-free (H<sub>2</sub>O, GO,  
724 Coffee) and Ag-containing (AgNPs, AgNPs/r-GO#<sub>1</sub>, and AgNPs/r-GO#<sub>2</sub>) samples when kept in the dark  
725 and under blue light irradiation at 9.5 mW.cm<sup>-2</sup>.

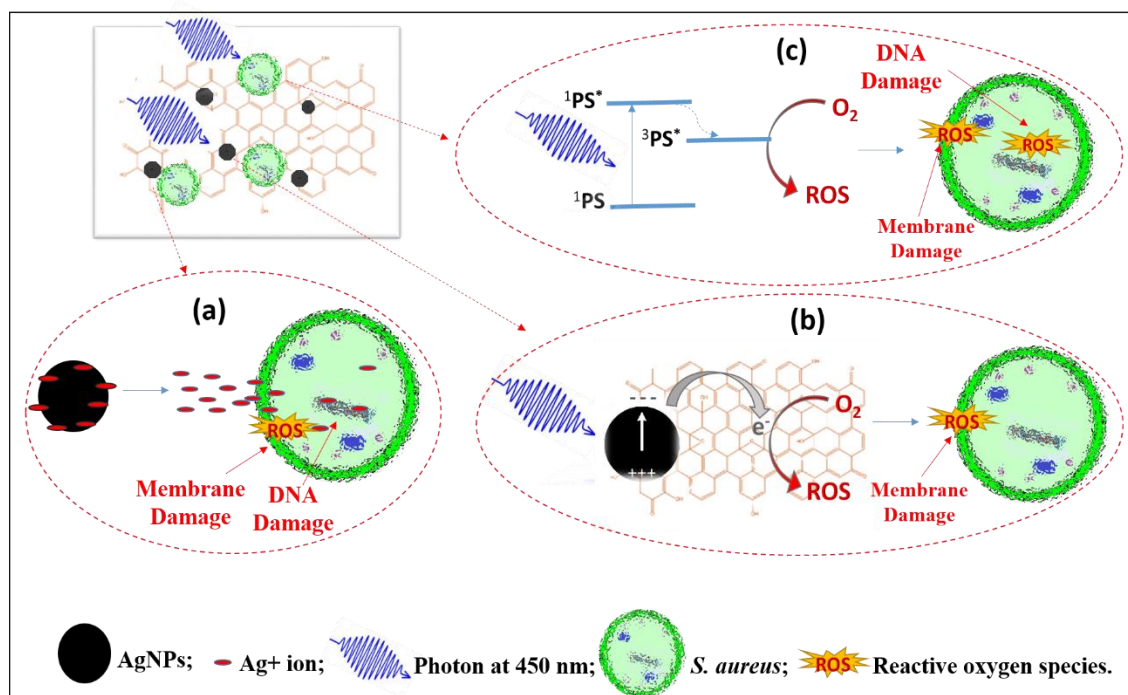
726 Although several studies have reported that porphyrins are the main endogenous  
727 photosensitizers to photoinactivate *S. aureus* strains under blue-light irradiation [104–106], our  
728 findings revealed that flavins are the key endogenous intracellular photosensitizers under 450  
729 nm illumination. As can be seen in Fig. 10, the bacterial extract has a broad fluorescence band  
730 in the 500 to 750 nm range with a maximum at around 530 nm due to the emission of the  
731 endogenous flavins and porphyrins extracted from bacterial cells. Fig. 10 also shows the  
732 fluorescence spectra of protoporphyrin IX and riboflavin when excited at 450 nm, which  
733 presents the typical emission spectra of porphyrins and flavins in the red (with maxima 630 nm  
734 and 695 nm) and green (with a maximum at 530 nm), respectively. By comparing the spectra  
735 profiles presented in Fig. 10, our data show that despite the presence of porphyrins and flavins  
736 in the bacterial extract, the flavins are the main endogenous photosensitizer present in the  
737 bacterial extract obtained from *S. aureus* strain. In addition to the spectral shape, the results

738 also demonstrated that the fluorescence intensity of porphyrins (with emission in the 625 to  
739 750 nm range) was very low, representing less than 80% of the bacterial extract emission. Our  
740 results are in accordance with similar findings presented by Plavskii and collaborators (2018)  
741 [107], which recently demonstrated that the presence of porphyrins was found in trace amounts  
742 in *S. aureus* extracts and also observed a maximum fluorescence band in the range of at around  
743 525 nm due to the presence of flavin compounds. Finally, it is important to stress that the main  
744 role played by flavins as endogenous photosensitizers is also because they present a maximum  
745 of absorption at around 450 nm, with a good overlap with the used photoactivation blue-light  
746 (with a maximum at 450 nm), as shown in Fig. S12 of the supplementary material, while the  
747 absorption bands of porphyrins have almost no overlap with this excitation light. Recent studies  
748 have demonstrated that the direct photoinactivation of bacteria by visible light strongly depends  
749 on the light wavelength, where the antibacterial effect promoted by blue light in the spectral  
750 range of 450–470 nm is mainly attributed to flavins, while porphyrins are mainly  
751 photoactivated by blue-light in the 400 to 430 nm range [108–110]. Lastly, our findings also  
752 demonstrated that the antibacterial effect of the blue-light photoactivated endogenous  
753 photosensitizers was primarily due to the disruption of the bacterial cell wall (Fig. S11) as well  
754 as the oxidation of intracellular DNA (Line 8) (Fig. 6).”



755  
 756 **Figure 10** - Fluorescence spectra of bacterial extract (solid line), riboflavin (dotted line), and  
 757 protoporphyrin IX (dotted-dashed line) when excited at 450 nm.  
 758

759 In fact, our findings demonstrated that the green synthesized silver nanoparticles  
 760 loaded on reduced graphene oxide sheets were effective on killing *S. aureus* under blue-  
 761 light irradiation (@450 nm), promoted by three different and simultaneous bacterial  
 762 killing mechanisms: (a)  $\text{Ag}^+$  ion release; (b) enhanced photoinactivation promoted by  
 763 excited-Plasmons of the AgNPs when anchored on r-GO; and (c) blue-light  
 764 photodynamic inactivation caused by bacterial endogenous photosensitizers, as is  
 765 schematically represented in Fig. 11. Finally, it is important to state that despite recent  
 766 studies have demonstrated that GO can promote an antibacterial effect induced by a  
 767 photothermal process under red and infrared light irradiation [100,111], no heating was  
 768 observed during the sample illumination in the present work. This result is in accordance  
 769 with Plavskii et al. [107], which demonstrated that even using higher light doses, the  
 770 photobactericidal effect promoted by the blue-light presented a photochemical but not a  
 771 photothermal nature.



772

773 **Figure 11** - Schematic diagram of antibacterial mechanisms induced by AgNPs/r-GO composites. (a)  
 774 Ag<sup>+</sup> ion release; (b) enhanced photoinactivation induce by excited-plasmons of the AgNPs loaded on r-  
 775 GO; and (c) blue-light antimicrobial photodynamic inactivation promoted by endogenous  
 776 photosensitizers.

777

#### 778 4. Conclusions

779 AgNPs/r-GO composites were prepared by an environmentally-friendly, simple,  
 780 inexpensive and non-toxic reaction set-up with a satisfactory yield of > 70% for silver  
 781 reduction. Our green method has the advantage that the r-GO surface acts as a suitable  
 782 platform for deposition of AgNPs to form composites for bio-related applications, using  
 783 coffee extract as a green reductant for both Ag<sup>+</sup> ions and GO reduction. AgNPs with a  
 784 mean diameter of about 70 nm were obtained for all Ag-containing samples (i.e., free  
 785 AgNPs and AgNPs anchored on the r-GO surface). The chemical characterization  
 786 showed that the silver was obtained in the metallic form with little oxidation at the  
 787 surface as evidenced by SAED and XPS. In addition, AgNPs were intimately linked to

788 the r-GO surface, with a negative Zeta potential that increased in modulus after the  
789 AgNPs/r-GO composite formation. The results also demonstrated that all Ag-containing  
790 samples (AgNPs, AgNPs/r-GO<sub>#1</sub> and AgNPs/r-GO<sub>#2</sub>) presented similar Ag<sup>+</sup> release rates  
791 of approx. 0.026 h<sup>-1</sup> that reflected in an excellent antibacterial effect against *S. aureus*.  
792 A reduction of approximately 2 logs in the bacterial counts was promoted for Ag-  
793 containing samples after 3h of interaction with the bacteria, and a bacterial inhibition  
794 growth over 99.9% after 6h was obtained with no significant difference among the  
795 samples. In addition, a clear antibacterial photodynamic inactivation was observed for  
796 all Ag-based materials after 45 min of blue light irradiation (at 20.3 J.cm<sup>-2</sup>) when  
797 compared with the Ag-free samples (H<sub>2</sub>O, GO, and coffee), which a statistically  
798 significant bacterial growth reduction of 88.6, 94.3 and 92.7% was observed for AgNPs,  
799 AgNPs/GO<sub>#1</sub> and AgNPs/GO<sub>#2</sub>, respectively. In addition, the photodynamic  
800 experiments also revealed that blue light irradiation was able to induce a  
801 photoantibacterial effect through photoactivation of endogenous photosensitizers; a  
802 bacterial growth reduction of ~ 99.4 % was determined for the Ag-free samples when  
803 irradiated at 51.3 J.cm<sup>-2</sup>. In summary, the present findings demonstrate that an efficient  
804 process of bacterial inactivation can be achieved using green synthesized AgNPs/r-GO  
805 compounds as a consequence of the Ag<sup>+</sup> ion release (chemical antibacterial effect) and  
806 the enhanced photoinactivation promoted by excited-Plasmons of the AgNPs when  
807 anchored on rGO in association with the blue-light photodynamic inactivation caused  
808 by bacterial endogenous photosensitizers (photodynamic antibacterial effects).

809

#### 810 **Conflicts of interest**

811 There are no conflicts to declare.

812

813 **Statement of contributions**

814 C.S.A. Caires performed the bactericidal and photobactericidal experiments; L.A.S. Farias and  
815 L.E. Gomes contributed to the development of the AgNPs-r-GO composites, UV-Vis and DLS  
816 measurements; B.P. Pinto and D.C.B. Alves helped with the graphene oxide preparation and  
817 Raman characterization; D.A. Gonçalves and V.A. Nascimento carried out ICP-OES  
818 characterization and ion release experiments; L.F. Zagonel made the microscopy analyzes; I.  
819 Colbeck and C. Whitby analyzed the results and review the manuscript; A.R.L. Caires and H.  
820 Wender conceived this research, analyzed the results, wrote the manuscript and supervised the  
821 entire project. All authors have given approval to the final version of the manuscript.

822

823 **Acknowledgements**

824 This study was supported by Universidade Federal de Mato Grosso do Sul –  
825 UFMS/MEC – Brasil and also financed in part by the Coordenação de Aperfeiçoamento  
826 de Pessoal de Nível Superior - Brasil (CAPES) - Finance Code 001. The authors  
827 acknowledge the financial support provided by the CAPES-PrInt funding program  
828 (grant numbers: 88887.353061/2019-00, 88887.363131/2019-00, 88881.311921/2018-  
829 01 and 88887.311920/2018-00) and the National Institute of Science and Technology  
830 of Basic Optics and Optics Applied to Life Science (grant number: 465360/2014-9). The  
831 authors are grateful to CNPq, CAPES and FUNDECT, Brazilian funding agencies, for  
832 their financial support. The authors also would like to acknowledge C.M. Silva, A.R.  
833 Lima, L.O. Araujo, L.M. Alves, and F. Benyahia for their technical support, and  
834 Professor Renato Gonçalves (IFSC-USP) for providing access to the XPS and micro-  
835 Raman equipment.

836 **References**

837 [1] S. Priyadarsini, S. Mukherjee, M. Mishra, Nanoparticles used in dentistry: A review, J.

- 838 Oral Biol. Craniofacial Res. 8 (2018) 58–67. doi:10.1016/j.jobcr.2017.12.004.
- 839 [2] A. Shrestha, A. Kishen, Antibacterial Nanoparticles in Endodontics: A Review, J.
- 840 Endod. 42 (2016) 1417–1426. doi:10.1016/j.joen.2016.05.021.
- 841 [3] S.P. Deshmukh, S.M. Patil, S.B. Mullani, S.D. Delekar, Silver nanoparticles as an
- 842 effective disinfectant: A review, Mater. Sci. Eng. C. 97 (2019) 954–965.
- 843 doi:10.1016/j.msec.2018.12.102.
- 844 [4] M.N. Nadagouda, R.S. Varma, Green synthesis of silver and palladium nanoparticles
- 845 at room temperature using coffee and tea extract, Green Chem. 10 (2008) 859.
- 846 doi:10.1039/b804703k.
- 847 [5] M. Amin, F. Anwar, M.R.S.A. Janjua, M.A. Iqbal, U. Rashid, Green synthesis of silver
- 848 nanoparticles through reduction with *Solanum xanthocarpum* L. berry extract:
- 849 Characterization, antimicrobial and urease inhibitory activities against *Helicobacter*
- 850 *pylori*, Int. J. Mol. Sci. 13 (2012) 9923–9941. doi:10.3390/ijms13089923.
- 851 [6] S.W. Chook, C.H. Chia, S. Zakaria, M.K. Ayob, K.L. Chee, N.M. Huang, H.M. Neoh,
- 852 H.N. Lim, R. Jamal, R.M.F.R.A. Rahman, Antibacterial performance of Ag
- 853 nanoparticles and AgGO nanocomposites prepared via rapid microwave-assisted
- 854 synthesis method, Nanoscale Res. Lett. 7 (2012) 1–7. doi:10.1186/1556-276X-7-541.
- 855 [7] J.J. Mock, M. Barbic, D.R. Smith, D.A. Schultz, S. Schultz, Shape effects in plasmon
- 856 resonance of individual colloidal silver nanoparticles, J. Chem. Phys. 116 (2002)
- 857 6755–6759. doi:10.1063/1.1462610.
- 858 [8] W.F. Falco, A.M. Queiroz, J. Fernandes, E.R. Botero, E.A. Falcão, F.E.G. Guimarães,
- 859 J.M. Peko, S.L. Oliveira, I. Colbeck, A.R.L. Caires, Journal of Photochemistry and
- 860 Photobiology A : Chemistry Interaction between chlorophyll and silver nanoparticles :
- 861 A close analysis of chlorophyll fluorescence quenching, 299 (2015) 203–209.
- 862 [9] V.K. Sharma, R.A. Yngard, Y. Lin, Silver nanoparticles: Green synthesis and their
- 863 antimicrobial activities, Adv. Colloid Interface Sci. 145 (2009) 83–96.
- 864 doi:10.1016/j.cis.2008.09.002.
- 865 [10] A. Kumar, P.K. Vemula, P.M. Ajayan, G. John, Silver-nanoparticle-embedded
- 866 antimicrobial paints based on vegetable oil, Nat. Mater. 7 (2008) 236–241.
- 867 doi:10.1038/nmat2099.
- 868 [11] Y. He, F. Wei, Z. Ma, H. Zhang, Q. Yang, B. Yao, Z. Huang, J. Li, C. Zeng, Q. Zhang,
- 869 Green synthesis of silver nanoparticles using seed extract of *Alpinia katsumadai*, and
- 870 their antioxidant, cytotoxicity, and antibacterial activities, RSC Adv. 7 (2017) 39842–
- 871 39851. doi:10.1039/C7RA05286C.
- 872 [12] S. Ahmed, Saifullah, M. Ahmad, B.L. Swami, S. Ikram, Green synthesis of silver
- 873 nanoparticles using *Azadirachta indica* aqueous leaf extract, J. Radiat. Res. Appl. Sci.
- 874 9 (2016) 1–7. doi:10.1016/j.jrras.2015.06.006.
- 875 [13] G. Gnanajobitha, S. Rajeshkumar, G. Annadurai, C. Kannan, Preparation and
- 876 characterization of fruit-mediated silver nanoparticles using pomegranate extract and
- 877 assessment of its antimicrobial activities, J. Environ. Nanotechnol. 2 (2013) 20–27.
- 878 doi:10.13074/jent.2013.02.121023.
- 879 [14] V. Dhand, L. Soumya, S. Bharadwaj, S. Chakra, D. Bhatt, B. Sreedhar, Green
- 880 synthesis of silver nanoparticles using *Coffea arabica* seed extract and its antibacterial
- 881 activity, Mater. Sci. Eng. C. 58 (2016) 36–43. doi:10.1016/j.msec.2015.08.018.
- 882 [15] L. Cardeño Calle, M.E. Londoño López, Green synthesis of silver nanoparticles using
- 883 green coffee bean extract, (2017) 217–220. doi:10.1007/978-981-10-4086-3\_55.
- 884 [16] J. Beddow, B. Stolpe, P. Cole, J.R. Lead, M. Sapp, B.P. Lyons, I. Colbeck, C. Whitby,
- 885 Effects of engineered silver nanoparticles on the growth and activity of ecologically
- 886 important microbes, Environ. Microbiol. Rep. 6 (2014) 448–458. doi:10.1111/1758-
- 887 2229.12147.

- 888 [17] K. Prasad, G.S. Lekshmi, K. Ostrikov, V. Lussini, J. Blinco, M. Mohandas, K. Vasilev,  
889 S. Bottle, K. Bazaka, K. Ostrikov, Synergic bactericidal effects of reduced graphene  
890 oxide and silver nanoparticles against Gram-positive and Gram-negative bacteria, *Sci.*  
891 *Rep.* 7 (2017) 1591. doi:10.1038/s41598-017-01669-5.
- 892 [18] J. Tanwar, S. Das, Z. Fatima, S. Hameed, Multidrug Resistance: An Emerging Crisis,  
893 *Interdiscip. Perspect. Infect. Dis.* 2014 (2014) 1–7. doi:10.1155/2014/541340.
- 894 [19] V.K. Sharma, N. Johnson, L. Cizmas, T.J. McDonald, H. Kim, A review of the  
895 influence of treatment strategies on antibiotic resistant bacteria and antibiotic  
896 resistance genes, *Chemosphere.* 150 (2016) 702–714.  
897 doi:10.1016/j.chemosphere.2015.12.084.
- 898 [20] H. Nikaido, Multidrug Resistance in Bacteria, *Annu. Rev. Biochem.* 78 (2009) 119–  
899 146. doi:10.1146/annurev.biochem.78.082907.145923.
- 900 [21] R.J. Worthington, C. Melander, Combination approaches to combat multidrug-  
901 resistant bacteria, *Trends Biotechnol.* 31 (2013) 177–184.  
902 doi:10.1016/j.tibtech.2012.12.006.
- 903 [22] H. Chandra, P. Bishnoi, A. Yadav, B. Patni, A. Mishra, A. Nautiyal, Antimicrobial  
904 Resistance and the Alternative Resources with Special Emphasis on Plant-Based  
905 Antimicrobials—A Review, *Plants.* 6 (2017) 16. doi:10.3390/plants6020016.
- 906 [23] M. Wainwright, T. Maisch, S. Nonell, K. Plaetzer, A. Almeida, G.P. Tegos, M.R.  
907 Hamblin, Photoantimicrobials—are we afraid of the light?, *Lancet Infect. Dis.* 17  
908 (2017) e49–e55. doi:10.1016/S1473-3099(16)30268-7.
- 909 [24] M. dos S. Vasconcelos, W.E. Passos, C.H. Lescanos, I. Pires de Oliveira, M.A.G.  
910 Trindade, A.R.L. Caires, R.M. Muzzi, Fluorescence Spectroscopy Applied to  
911 Monitoring Biodiesel Degradation: Correlation with Acid Value and UV Absorption  
912 Analyses, *J. Anal. Methods Chem.* 2018 (2018) 1–11. doi:10.1155/2018/4175843.
- 913 [25] M. Yousefi, M. Dadashpour, M. Hejazi, M. Hasanzadeh, B. Behnam, M. de la  
914 Guardia, N. Shadjou, A. Mokhtarzadeh, Anti-bacterial activity of graphene oxide as a  
915 new weapon nanomaterial to combat multidrug-resistance bacteria, *Mater. Sci. Eng. C.*  
916 74 (2017) 568–581. doi:10.1016/j.msec.2016.12.125.
- 917 [26] C.S.A. Caires, C.R.B. Leal, C.A.N. Ramos, D. Bogo, A.R. Lima, E.J. Arruda, S.L.  
918 Oliveira, A.R.L. Caires, V.A. Nascimento, Photoinactivation effect of eosin methylene  
919 blue and chlorophyllin sodium-copper against *Staphylococcus aureus* and *Escherichia*  
920 *coli*, *Lasers Med. Sci.* 32 (2017). doi:10.1007/s10103-017-2210-1.
- 921 [27] C.S.A. Caires, C.R.B. Leal, A.C.S. Rodrigues, A.R. Lima, C.M. Silva, C.A.N. Ramos,  
922 M.R. Chang, E.J. Arruda, S.L. Oliveira, V.A. Nascimento, A.R.L. Caires,  
923 Photoinactivation of *mcr-1* positive *Escherichia coli*, *Laser Phys. Lett.* 15 (2018).  
924 doi:10.1088/1612-202X/aa86e0.
- 925 [28] J. Liu, M.D. Rojas-Andrade, G. Chata, Y. Peng, G. Roseman, J.-E. Lu, G.L.  
926 Millhauser, C. Saltikov, S. Chen, Photo-enhanced antibacterial activity of  
927 ZnO/graphene quantum dot nanocomposites, *Nanoscale.* 10 (2018) 158–166.  
928 doi:10.1039/C7NR07367D.
- 929 [29] R. Babu, J. Zhang, E.J. Beckman, M. Virji, W.A. Pasculle, A. Wells, Antimicrobial  
930 activities of silver used as a polymerization catalyst for a wound-healing matrix,  
931 *Biomaterials.* 27 (2006) 4304–4314. doi:10.1016/j.biomaterials.2006.03.038.
- 932 [30] Q.L. Feng, J. Wu, G.Q. Chen, F.Z. Cui, T.N. Kim, J.O. Kim, A mechanistic study of  
933 the antibacterial effect of silver ions on *Escherichia coli* and *Staphylococcus aureus*, *J.*  
934 *Biomed. Mater. Res.* 52 (2000) 662–668. doi:10.1002/1097-  
935 4636(20001215)52:4<662::AID-JBM10>3.0.CO;2-3.
- 936 [31] W.S. Hummers, R.E. Offeman, Preparation of Graphitic Oxide, *J. Am. Chem. Soc.* 80  
937 (1958) 1339. doi:10.1021/ja01539a017.

- 938 [32] M. Roushani, Z. Rahmati, S. Farokhi, S.J. Hoseini, R.H. Fath, The development of an  
939 electrochemical nanoaptasensor to sensing chloramphenicol using a nanocomposite  
940 consisting of graphene oxide functionalized with (3-Aminopropyl) triethoxysilane and  
941 silver nanoparticles, *Mater. Sci. Eng. C.* 108 (2020) 110388.  
942 doi:10.1016/j.msec.2019.110388.
- 943 [33] J. Peng, J. Lin, Z. Chen, M. Wei, Y. Fu, S. Lu, D. Yu, W. Zhao, Enhanced  
944 antimicrobial activities of silver-nanoparticle-decorated reduced graphene  
945 nanocomposites against oral pathogens, *Mater. Sci. Eng. C.* 71 (2017) 10–16.  
946 doi:10.1016/j.msec.2016.09.070.
- 947 [34] T. Arun, S.K. Verma, P.K. Panda, R.J. Joseyphus, E. Jha, A. Akbari-Fakhrabadi, P.  
948 Sengupta, D.K. Ray, V.S. Benitha, K. Jeyasubramanian, P.V. Satyam, Facile  
949 synthesized novel hybrid graphene oxide/cobalt ferrite magnetic nanoparticles based  
950 surface coating material inhibit bacterial secretion pathway for antibacterial effect,  
951 *Mater. Sci. Eng. C.* 104 (2019) 109932. doi:10.1016/j.msec.2019.109932.
- 952 [35] S.S. Nanda, G.C. Papaefthymiou, D.K. Yi, Functionalization of Graphene Oxide and  
953 its Biomedical Applications, *Crit. Rev. Solid State Mater. Sci.* 40 (2015) 291–315.  
954 doi:10.1080/10408436.2014.1002604.
- 955 [36] J. Tang, Q. Chen, L. Xu, S. Zhang, L. Feng, L. Cheng, H. Xu, Z. Liu, R. Peng,  
956 Graphene oxide-silver nanocomposite as a highly effective antibacterial agent with  
957 species-specific mechanisms, *ACS Appl. Mater. Interfaces.* 5 (2013) 3867–3874.  
958 doi:10.1021/am4005495.
- 959 [37] A. El-Hussein, M.R. Hamblin, ROS generation and DNA damage with photo-  
960 inactivation mediated by silver nanoparticles in lung cancer cell line, *IET*  
961 *Nanobiotechnology.* 11 (2017) 173–178. doi:10.1049/iet-nbt.2015.0083.
- 962 [38] X. Xie, C. Mao, X. Liu, Y. Zhang, Z. Cui, X. Yang, K.W.K. Yeung, H. Pan, P.K. Chu,  
963 S. Wu, Synergistic Bacteria Killing through Photodynamic and Physical Actions of  
964 Graphene Oxide/Ag/Collagen Coating, *ACS Appl. Mater. Interfaces.* 9 (2017) 26417–  
965 26428. doi:10.1021/acsami.7b06702.
- 966 [39] X. Chen, X. Huang, C. Zheng, Y. Liu, T. Xu, J. Liu, Preparation of different sized  
967 nano-silver loaded on functionalized graphene oxide with highly effective antibacterial  
968 properties, *J. Mater. Chem. B.* 3 (2015) 7020–7029. doi:10.1039/C5TB00280J.
- 969 [40] D. Xia, T. An, G. Li, W. Wang, H. Zhao, P.K. Wong, Synergistic photocatalytic  
970 inactivation mechanisms of bacteria by graphene sheets grafted plasmonic Ag AgX (X  
971 = Cl, Br, I) composite photocatalyst under visible light irradiation, *Water Res.* 99  
972 (2016) 149–161. doi:10.1016/j.watres.2016.04.055.
- 973 [41] A. Besinis, T. De Peralta, R.D. Handy, The antibacterial effects of silver, titanium  
974 dioxide and silica dioxide nanoparticles compared to the dental disinfectant  
975 chlorhexidine on *Streptococcus mutans* using a suite of bioassays, *Nanotoxicology.* 8  
976 (2014) 1–16. doi:10.3109/17435390.2012.742935.
- 977 [42] M.D. Scherer, J.C.V. Sposito, W.F. Falco, A.B. Grisolia, L.H.C. Andrade, S.M. Lima,  
978 G. Machado, V.A. Nascimento, D.A. Gonçalves, H. Wender, S.L. Oliveira, A.R.L.  
979 Caires, Cytotoxic and genotoxic effects of silver nanoparticles on meristematic cells of  
980 *Allium cepa* roots: A close analysis of particle size dependence, *Sci. Total Environ.*  
981 660 (2019) 459–467. doi:10.1016/j.scitotenv.2018.12.444.
- 982 [43] J. Hui, Z.J. O'Dell, A. Rao, K.R. Riley, In Situ Quantification of Silver Nanoparticle  
983 Dissolution Kinetics in Simulated Sweat Using Linear Sweep Stripping Voltammetry,  
984 *Environ. Sci. Technol.* (2019) acs.est.9b04151. doi:10.1021/acs.est.9b04151.
- 985 [44] W. Zhang, Y. Yao, N. Sullivan, Y. Chen, Modeling the Primary Size Effects of  
986 Citrate-Coated Silver Nanoparticles on Their Ion Release Kinetics, *Environ. Sci.*  
987 *Technol.* 45 (2011) 4422–4428. doi:10.1021/es104205a.

- 988 [45] J. Liu, R.H. Hurt, Ion Release Kinetics and Particle Persistence in Aqueous Nano-  
989 Silver Colloids, *Environ. Sci. Technol.* 44 (2010) 2169–2175. doi:10.1021/es9035557.
- 990 [46] X. Chen, Z. Zhong, Z. Xu, L. Chen, Y. Wang, 2',7'-Dichlorodihydrofluorescein as a  
991 fluorescent probe for reactive oxygen species measurement: Forty years of application  
992 and controversy, *Free Radic. Res.* 44 (2010) 587–604.  
993 doi:10.3109/10715761003709802.
- 994 [47] Y. Wen, L. Zhang, Z. Chen, X. Sheng, J. Qiu, D. Xu, Co-exposure of silver  
995 nanoparticles and chiral herbicide imazethapyr to *Arabidopsis thaliana*:  
996 Enantioselective effects, *Chemosphere.* 145 (2016) 207–214.  
997 doi:10.1016/j.chemosphere.2015.11.035.
- 998 [48] R.I. Griffiths, A.S. Whiteley, A.G. O'Donnell, M.J. Bailey, Rapid Method for  
999 Coextraction of DNA and RNA from Natural Environments for Analysis of Ribosomal  
1000 DNA- and rRNA-Based Microbial Community Composition, *Appl. Environ.*  
1001 *Microbiol.* 66 (2000) 5488–5491. doi:10.1128/AEM.66.12.5488-5491.2000.
- 1002 [49] D. Liu, M.L. Lawrence, F.W. Austin, Evaluation of PCR primers from putative  
1003 transcriptional regulator genes for identification of *Staphylococcus aureus*, *Lett. Appl.*  
1004 *Microbiol.* 40 (2005) 69–73. doi:10.1111/j.1472-765X.2004.01629.x.
- 1005 [50] S. Mancini, J. Imlay, Bacterial Porphyrin Extraction and Quantification by LC/MS/MS  
1006 Analysis, *BIO-PROTOCOL.* 5 (2015). doi:10.21769/BioProtoc.1616.
- 1007 [51] A.S. Al-Sherbini, M. Bakr, I. Ghoneim, M. Saad, Exfoliation of graphene sheets via  
1008 high energy wet milling of graphite in 2-ethylhexanol and kerosene, *J. Adv. Res.* 8  
1009 (2017) 209–215. doi:10.1016/j.jare.2017.01.004.
- 1010 [52] J. Kim, F. Kim, J. Huang, Seeing graphene-based sheets, *Mater. Today.* 13 (2010) 28–  
1011 38. doi:10.1016/S1369-7021(10)70031-6.
- 1012 [53] M. Vinothkannan, C. Karthikeyan, G. Gnana Kumar, A.R. Kim, D.J. Yoo, One-pot  
1013 green synthesis of reduced graphene oxide (RGO)/Fe<sub>3</sub>O<sub>4</sub> nanocomposites and its  
1014 catalytic activity toward methylene blue dye degradation, *Spectrochim. Acta - Part A*  
1015 *Mol. Biomol. Spectrosc.* 136 (2015) 256–264. doi:10.1016/j.saa.2014.09.031.
- 1016 [54] K.S. Divya, A. Chandran, V.N. Reethu, S. Mathew, Enhanced photocatalytic  
1017 performance of RGO/Ag nanocomposites produced via a facile microwave irradiation  
1018 for the degradation of Rhodamine B in aqueous solution, *Appl. Surf. Sci.* 444 (2018)  
1019 811–818. doi:10.1016/j.apsusc.2018.01.303.
- 1020 [55] N. Wu, X. She, D. Yang, X. Wu, F. Su, Y. Chen, Synthesis of network reduced  
1021 graphene oxide in polystyrene matrix by a two-step reduction method for superior  
1022 conductivity of the composite, *J. Mater. Chem.* 22 (2012) 17254.  
1023 doi:10.1039/c2jm33114d.
- 1024 [56] W. Yuan, Y. Gu, L. Li, Green synthesis of graphene/Ag nanocomposites, *Appl. Surf.*  
1025 *Sci.* 261 (2012) 753–758. doi:10.1016/j.apsusc.2012.08.094.
- 1026 [57] S. Liu, J. Tian, L. Wang, X. Sun, A method for the production of reduced graphene  
1027 oxide using benzylamine as a reducing and stabilizing agent and its subsequent  
1028 decoration with Ag nanoparticles for enzymeless hydrogen peroxide detection, *Carbon*  
1029 *N. Y.* 49 (2011) 3158–3164. doi:10.1016/j.carbon.2011.03.036.
- 1030 [58] T.H. Joo, M.S. Kim, K. Kim, Surface-enhanced Raman scattering of benzenethiol in  
1031 silver sol, *J. Raman Spectrosc.* 18 (1987) 57–60. doi:10.1002/jrs.1250180111.
- 1032 [59] T.A. Saleh, M.M. Al-Shalalfeh, A.A. Al-Saadi, Silver nanoparticles for detection of  
1033 methimazole by surface-enhanced Raman spectroscopy, *Mater. Res. Bull.* 91 (2017)  
1034 173–178. doi:10.1016/j.materresbull.2017.03.041.
- 1035 [60] L. Tao, Y. Lou, Y. Zhao, M. Hao, Y. Yang, Y. Xiao, Y.H. Tsang, J. Li, Silver  
1036 nanoparticle-decorated graphene oxide for surface-enhanced Raman scattering  
1037 detection and optical limiting applications, *J. Mater. Sci.* 53 (2018) 573–580.

- doi:10.1007/s10853-017-1501-z.
- 1038  
1039 [61] M. Gühlke, Z. Heiner, J. Kneipp, Surface-Enhanced Raman and Surface-Enhanced  
1040 Hyper-Raman Scattering of Thiol-Functionalized Carotene, *J. Phys. Chem. C*. 120  
1041 (2016) 20702–20709. doi:10.1021/acs.jpcc.6b01895.
- 1042 [62] X. Liao, Y. Chen, M. Qin, Y. Chen, L. Yang, H. Zhang, Y. Tian, Au–Ag–Au double  
1043 shell nanoparticles-based localized surface plasmon resonance and surface-enhanced  
1044 Raman scattering biosensor for sensitive detection of 2-mercapto-1-methylimidazole,  
1045 *Talanta*. 117 (2013) 203–208. doi:10.1016/j.talanta.2013.08.051.
- 1046 [63] A. Soroush, W. Ma, Y. Silvino, M.S. Rahaman, Surface modification of thin film  
1047 composite forward osmosis membrane by silver-decorated graphene-oxide nanosheets,  
1048 *Environ. Sci. Nano*. 2 (2015) 395–405. doi:10.1039/C5EN00086F.
- 1049 [64] S. Thakur, N. Karak, Green reduction of graphene oxide by aqueous phytoextracts,  
1050 *Carbon N. Y.* 50 (2012) 5331–5339. doi:10.1016/j.carbon.2012.07.023.
- 1051 [65] M. Navya Rani, S. Ananda, D. Rangappa, Preparation of Reduced Graphene Oxide  
1052 and Its Antibacterial Properties, *Mater. Today Proc.* 4 (2017) 12300–12305.  
1053 doi:10.1016/j.matpr.2017.09.163.
- 1054 [66] M.J.-Y. Tai, W.-W. Liu, C.-S. Khe, N.M.S. Hidayah, Y.-P. Teoh, C.H. Voon, H.C.  
1055 Lee, P.Y.P. Adelyn, Green synthesis of reduced graphene oxide using green tea  
1056 extract, in: 2018: p. 020032. doi:10.1063/1.5080845.
- 1057 [67] L. Liu, J. Liu, Y. Wang, X. Yan, D.D. Sun, Facile synthesis of monodispersed silver  
1058 nanoparticles on graphene oxide sheets with enhanced antibacterial activity, *New J.*  
1059 *Chem.* 35 (2011) 1418. doi:10.1039/c1nj20076c.
- 1060 [68] X. Chen, B. Su, G. Wu, C.J. Yang, Z. Zhuang, X. Wang, X. Chen, Platinum  
1061 nanoflowers supported on graphene oxide nanosheets: their green synthesis, growth  
1062 mechanism, and advanced electrocatalytic properties for methanol oxidation, *J. Mater.*  
1063 *Chem.* 22 (2012) 11284. doi:10.1039/c2jm31133j.
- 1064 [69] X. Wang, H. Bai, G. Shi, Size Fractionation of Graphene Oxide Sheets by pH-Assisted  
1065 Selective Sedimentation, *J. Am. Chem. Soc.* 133 (2011) 6338–6342.  
1066 doi:10.1021/ja200218y.
- 1067 [70] Y. Feng, K.A. Huynh, Z. Xie, G. Liu, S. Gao, Heteroaggregation and sedimentation of  
1068 graphene oxide with hematite colloids: Influence of water constituents and impact on  
1069 tetracycline adsorption, *Sci. Total Environ.* 647 (2019) 708–715.  
1070 doi:10.1016/j.scitotenv.2018.08.046.
- 1071 [71] C. Rodríguez-González, P. Velázquez-Villalba, P. Salas, V.M. Castaño, Green  
1072 synthesis of nanosilver-decorated graphene oxide sheets, *IET Nanobiotechnology*. 10  
1073 (2016) 301–307. doi:10.1049/iet-nbt.2015.0043.
- 1074 [72] M.Z. Ansari, M.A. Wahid, R. Johari, M.A. Qureshi, W.A. Siddiqi, Novel honey  
1075 mediated green synthesis of Graphene@Ag Nanocomposite and its two-dimensional  
1076 application in photovoltaic and anti-microbial activity, *Mater. Res. Express*. 6 (2019)  
1077 115071. doi:10.1088/2053-1591/ab4a64.
- 1078 [73] R. Desai, V. Mankad, S. Gupta, P. Jha, Size Distribution of Silver Nanoparticles: UV-  
1079 Visible Spectroscopic Assessment, *Nanosci. Nanotechnol. Lett.* 4 (2012) 30–34.  
1080 doi:10.1166/nnl.2012.1278.
- 1081 [74] S. Saxena, T.A. Tyson, S. Shukla, E. Negusse, H. Chen, J. Bai, Investigation of  
1082 structural and electronic properties of graphene oxide, *Appl. Phys. Lett.* 99 (2011)  
1083 013104. doi:10.1063/1.3607305.
- 1084 [75] D.K. Bhui, H. Bar, P. Sarkar, G.P. Sahoo, S.P. De, A. Misra, Synthesis and UV-vis  
1085 spectroscopic study of silver nanoparticles in aqueous SDS solution, *J. Mol. Liq.* 145  
1086 (2009) 33–37. doi:10.1016/j.molliq.2008.11.014.
- 1087 [76] J.M. Ashraf, M.A. Ansari, H.M. Khan, M.A. Alzohairy, I. Choi, Green synthesis of

- 1088 silver nanoparticles and characterization of their inhibitory effects on AGEs formation  
 1089 using biophysical techniques, *Sci. Rep.* 6 (2016) 1–10. doi:10.1038/srep20414.
- 1090 [77] B. Tewabe Gebeyehu, Determination of Caffeine Content and Antioxidant Activity of  
 1091 Coffee, *Am. J. Appl. Chem.* 3 (2015) 69. doi:10.11648/j.ajac.20150302.16.
- 1092 [78] A. Belay, K. Ture, M. Redi, A. Asfaw, Measurement of caffeine in coffee beans with  
 1093 UV/vis spectrometer, *Food Chem.* 108 (2008) 310–315.  
 1094 doi:10.1016/j.foodchem.2007.10.024.
- 1095 [79] G. Navarra, M. Moschetti, V. Guarrasi, M.R. Mangione, V. Militello, M. Leone,  
 1096 Simultaneous Determination of Caffeine and Chlorogenic Acids in Green Coffee by  
 1097 UV/Vis Spectroscopy, *J. Chem.* 2017 (2017) 1–8. doi:10.1155/2017/6435086.
- 1098 [80] S. Bhattacharjee, DLS and zeta potential - What they are and what they are not?, *J.*  
 1099 *Control. Release.* 235 (2016) 337–351. doi:10.1016/j.jconrel.2016.06.017.
- 1100 [81] B. Tang, X. Hou, J. Li, M. Zhang, L. Sun, X. Wang, Acceleration effect of reduced  
 1101 graphene oxide on photoinduced synthesis of silver nanoparticles, *Phys. Chem. Chem.*  
 1102 *Phys.* 15 (2013) 11106. doi:10.1039/c3cp44312d.
- 1103 [82] R. Geetha Bai, K. Muthoosamy, F.N. Shipton, A. Pandikumar, P. Rameshkumar, N.M.  
 1104 Huang, S. Manickam, The biogenic synthesis of a reduced graphene oxide–silver  
 1105 (RGO–Ag) nanocomposite and its dual applications as an antibacterial agent and  
 1106 cancer biomarker sensor, *RSC Adv.* 6 (2016) 36576–36587.  
 1107 doi:10.1039/C6RA02928K.
- 1108 [83] A.M. Shanmugaraj, S.H. Ryu, Excellent electrochemical performance of graphene-  
 1109 silver nanoparticle hybrids prepared using a microwave spark assistance process,  
 1110 *Electrochim. Acta.* 74 (2012) 207–214. doi:10.1016/j.electacta.2012.04.057.
- 1111 [84] G. Beamson, D. Briggs, High Resolution XPS of Organic Polymers - The Scienta  
 1112 ESCA300 Database, Wiley Interscience, 1992.
- 1113 [85] A.M. Ferraria, A.P. Carapeto, A.M. Botelho do Rego, X-ray photoelectron  
 1114 spectroscopy: Silver salts revisited, *Vacuum.* 86 (2012) 1988–1991.  
 1115 doi:10.1016/j.vacuum.2012.05.031.
- 1116 [86] V.T.H. Pham, V.K. Truong, M.D.J. Quinn, S.M. Notley, Y. Guo, V.A. Baulin, M. Al  
 1117 Kobaisi, R.J. Crawford, E.P. Ivanova, Graphene Induces Formation of Pores That Kill  
 1118 Spherical and Rod-Shaped Bacteria, *ACS Nano.* 9 (2015) 8458–8467.  
 1119 doi:10.1021/acs.nano.5b03368.
- 1120 [87] M.D. Rojas-Andrade, G. Chata, D. Rouholiman, J. Liu, C. Saltikov, S. Chen,  
 1121 Antibacterial mechanisms of graphene-based composite nanomaterials, *Nanoscale.* 9  
 1122 (2017) 994–1006. doi:10.1039/C6NR08733G.
- 1123 [88] X. Zou, L. Zhang, Z. Wang, Y. Luo, Mechanisms of the Antimicrobial Activities of  
 1124 Graphene Materials, *J. Am. Chem. Soc.* 138 (2016) 2064–2077.  
 1125 doi:10.1021/jacs.5b11411.
- 1126 [89] H. Zheng, R. Ma, M. Gao, X. Tian, Y.-Q. Li, L. Zeng, R. Li, Antibacterial applications  
 1127 of graphene oxides: structure-activity relationships, molecular initiating events and  
 1128 biosafety, *Sci. Bull.* 63 (2018) 133–142. doi:10.1016/j.scib.2017.12.012.
- 1129 [90] O. Akhavan, E. Ghaderi, Toxicity of Graphene and Graphene Oxide Nanowalls  
 1130 Against Bacteria, *ACS Nano.* 4 (2010) 5731–5736. doi:10.1021/nn101390x.
- 1131 [91] F. Perreault, A.F. de Faria, S. Nejati, M. Elimelech, Antimicrobial Properties of  
 1132 Graphene Oxide Nanosheets: Why Size Matters, *ACS Nano.* 9 (2015) 7226–7236.  
 1133 doi:10.1021/acs.nano.5b02067.
- 1134 [92] W. Han, Z. Wu, Y. Li, Y. Wang, Graphene family nanomaterials (GFNs)—promising  
 1135 materials for antimicrobial coating and film: A review, *Chem. Eng. J.* 358 (2019)  
 1136 1022–1037. doi:10.1016/j.cej.2018.10.106.
- 1137 [93] M.R. Das, R.K. Sarma, S.C. Borah, R. Kumari, R. Saikia, A.B. Deshmukh, M. V.

- 1138 Shelke, P. Sengupta, S. Szunerits, R. Boukherroub, The synthesis of citrate-modified  
 1139 silver nanoparticles in an aqueous suspension of graphene oxide nanosheets and their  
 1140 antibacterial activity, *Colloids Surfaces B Biointerfaces*. 105 (2013) 128–136.  
 1141 doi:10.1016/j.colsurfb.2012.12.033.
- [94] D.K. Chatterjee, L.S. Fong, Y. Zhang, Nanoparticles in photodynamic therapy: An  
 1143 emerging paradigm, *Adv. Drug Deliv. Rev.* 60 (2008) 1627–1637.  
 1144 doi:10.1016/j.addr.2008.08.003.
- [95] S.S. Lucky, K.C. Soo, Y. Zhang, Nanoparticles in Photodynamic Therapy, *Chem. Rev.*  
 1146 115 (2015) 1990–2042. doi:10.1021/cr5004198.
- [96] A. El-Hussein, I. Mfouo-Tynga, M. Abdel-Harith, H. Abrahamse, Comparative study  
 1147 between the photodynamic ability of gold and silver nanoparticles in mediating cell  
 1148 death in breast and lung cancer cell lines, *J. Photochem. Photobiol. B Biol.* 153 (2015)  
 1149 67–75. doi:10.1016/j.jphotobiol.2015.08.028.
- [97] L. Gao, R. Liu, F. Gao, Y. Wang, X. Jiang, X. Gao, Plasmon-Mediated Generation of  
 1151 Reactive Oxygen Species from Near-Infrared Light Excited Gold Nanocages for  
 1152 Photodynamic Therapy in Vitro, *ACS Nano*. 8 (2014) 7260–7271.  
 1153 doi:10.1021/nn502325j.
- [98] G. Afreen, M. Shoeb, S. Upadhyayula, Effectiveness of reactive oxygen species  
 1155 generated from rGO/CdS QD heterostructure for photodegradation and disinfection of  
 1156 pollutants in waste water, *Mater. Sci. Eng. C*. 108 (2020) 110372.  
 1157 doi:10.1016/j.msec.2019.110372.
- [99] M. Zhu, X. Liu, L. Tan, Z. Cui, Y. Liang, Z. Li, K.W. Kwok Yeung, S. Wu, Photo-  
 1159 responsive chitosan/Ag/MoS<sub>2</sub> for rapid bacteria-killing, *J. Hazard. Mater.* 383 (2020)  
 1160 121122. doi:10.1016/j.jhazmat.2019.121122.
- [100] Y. Li, X. Liu, L. Tan, Z. Cui, X. Yang, Y. Zheng, K.W.K. Yeung, P.K. Chu, S. Wu,  
 1162 Rapid Sterilization and Accelerated Wound Healing Using Zn<sup>2+</sup> and Graphene Oxide  
 1163 Modified g-C<sub>3</sub>N<sub>4</sub> under Dual Light Irradiation, *Adv. Funct. Mater.* 28 (2018)  
 1164 1800299. doi:10.1002/adfm.201800299.
- [101] X. Xie, C. Mao, X. Liu, L. Tan, Z. Cui, X. Yang, S. Zhu, Z. Li, X. Yuan, Y. Zheng,  
 1166 K.W.K. Yeung, P.K. Chu, S. Wu, Tuning the Bandgap of Photo-Sensitive  
 1167 Polydopamine/Ag<sub>3</sub>PO<sub>4</sub>/Graphene Oxide Coating for Rapid, Noninvasive  
 1168 Disinfection of Implants, *ACS Cent. Sci.* 4 (2018) 724–738.  
 1169 doi:10.1021/acscentsci.8b00177.
- [102] X. Wang, K. Su, L. Tan, X. Liu, Z. Cui, D. Jing, X. Yang, Y. Liang, Z. Li, S. Zhu,  
 1171 K.W.K. Yeung, D. Zheng, S. Wu, Rapid and Highly Effective Noninvasive  
 1172 Disinfection by Hybrid Ag/CS@MnO<sub>2</sub> Nanosheets Using Near-Infrared Light, *ACS*  
 1173 *Appl. Mater. Interfaces*. 11 (2019) 15014–15027. doi:10.1021/acsami.8b22136.
- [103] H. Lai, F. Xu, Y. Zhang, L. Wang, Recent progress on graphene-based substrates for  
 1175 surface-enhanced Raman scattering applications, *J. Mater. Chem. B*. 6 (2018) 4008–  
 1176 4028. doi:10.1039/C8TB00902C.
- [104] M. Maclean, S.J. MacGregor, J.G. Anderson, G.A. Woolsey, The role of oxygen in the  
 1178 visible-light inactivation of *Staphylococcus aureus*, *J. Photochem. Photobiol. B Biol.*  
 1179 92 (2008) 180–184. doi:10.1016/j.jphotobiol.2008.06.006.
- [105] T. Dai, A. Gupta, Y.-Y. Huang, M.E. Sherwood, C.K. Murray, M.S. Vrahas, T.  
 1181 Kielian, M.R. Hamblin, Blue Light Eliminates Community-Acquired Methicillin-  
 1182 Resistant *Staphylococcus aureus* in Infected Mouse Skin Abrasions, *Photomed. Laser*  
 1183 *Surg.* 31 (2013) 531–538. doi:10.1089/pho.2012.3365.
- [106] C.S. Enwemeka, D. Williams, S.K. Enwemeka, S. Hollosi, D. Yens, Blue 470-nm  
 1185 Light Kills Methicillin-Resistant *Staphylococcus aureus* (MRSA) in Vitro, *Photomed.*  
 1186 *Laser Surg.* 27 (2009) 221–226. doi:10.1089/pho.2008.2413.

- 1188 [107] V.Y. Plavskii, A.V. Mikulich, A.I. Tretyakova, I.A. Leusenka, L.G. Plavskaya, O.A.  
1189 Kazyuchits, I.I. Dobysh, T.P. Krasnenkova, Porphyrins and flavins as endogenous  
1190 acceptors of optical radiation of blue spectral region determining photoinactivation of  
1191 microbial cells, *J. Photochem. Photobiol. B Biol.* 183 (2018) 172–183.  
1192 doi:10.1016/j.jphotobiol.2018.04.021.
- 1193 [108] K. Hoenes, M. Hess, P. Vatter, B. Spellerberg, M. Hessling, 405 nm and 450 nm  
1194 photoinactivation of *Saccharomyces cerevisiae*, *Eur. J. Microbiol. Immunol.* 8 (2018)  
1195 142–148. doi:10.1556/1886.2018.00023.
- 1196 [109] Y. Wang, R. Ferrer-Espada, Y. Baglo, Y. Gu, T. Dai, Antimicrobial Blue Light  
1197 Inactivation of *Neisseria gonorrhoeae* : Roles of Wavelength, Endogenous  
1198 Photosensitizer, Oxygen, and Reactive Oxygen Species, *Lasers Surg. Med.* 51 (2019)  
1199 815–823. doi:10.1002/lsm.23104.
- 1200 [110] K. Hoenes, U. Wenzel, B. Spellerberg, M. Hessling, Photoinactivation Sensitivity of  
1201 *Staphylococcus carnosus* to Visible-light Irradiation as a Function of Wavelength,  
1202 *Photochem. Photobiol.* 96 (2020) 156–169. doi:10.1111/php.13168.
- 1203 [111] M.P. Romero, V.S. Marangoni, C.G. de Faria, I.S. Leite, C. de C.C. e Silva, C.M.  
1204 Maroneze, M.A. Pereira-da-Silva, V.S. Bagnato, N.M. Inada, Graphene Oxide  
1205 Mediated Broad-Spectrum Antibacterial Based on Bimodal Action of Photodynamic  
1206 and Photothermal Effects, *Front. Microbiol.* 10 (2020). doi:10.3389/fmicb.2019.02995.  
1207